Journal of Computational Physics 228 (2009) 3559–3581

Contents lists available at ScienceDirect

Journal of Computational Physics

journal homepage: www.elsevier.com/locate/jcp

Force-coupling method for flows with ellipsoidal particles

D. Liu [a], E.E. Keaveny [b], M.R. Maxey [b,*], G.E. Karniadakis [b]

[a] Department of Mathematics and Statistics, Louisiana Tech University, Ruston, LA 71272, United States
[b] Division of Applied Mathematics, Brown University, Providence, RI 02912, United States

ARTICLE INFO

Article history:
Received 20 August 2008
Received in revised form 9 January 2009
Accepted 19 January 2009
Available online 30 January 2009

Keywords:
Two-phase flow
Spectral element simulations
Direct numerical simulations

ABSTRACT

The force-coupling method, previously developed for spherical particles suspended in a liquid flow, is extended to ellipsoidal particles. In the limit of Stokes flow, there is an exact correspondence with known analytical results for isolated particles. More generally, the method is shown to provide good approximate results for the particle motion and the flow field both in viscous Stokes flow and at finite Reynolds number. This is demonstrated through comparison between fully resolved direct numerical simulations and results from the numerical implementation of the force-coupling method with a spectral/hp element scheme. The motion of settling ellipsoidal particles and neutrally buoyant particles in a Poiseuille flow are discussed.

1. Introduction

The development of microfluidic devices for sorting and analyzing particles has raised the need for effective simulation methods to determine the motion of small particles in confined flow systems. A general overview of the development of micro-electromechanical systems (MEMS) is given by Ho and Tai [1] and examples of particle separation for biochemical and biomedical analysis are given by Telleman et al. [2] and by Applegate et al. [3]. Often these devices involve complex geometries and a range of conditions for Reynolds number, particle size, concentration and possibly body forces (e.g. magnetic forces) acting on a particle. Magnetic fields, for instance, acting on super-paramagnetic beads provide a means for fabricating self-assembled structures such as particle chains carried by liquids in micro-channels [4–6]. Particles may also be used to promote mixing in micro-flows or to form the active element in pumping devices as shown experimentally by Terray et al. [7] and by Bleil et al. [8], and in simulations by Liu et al. [9].

Most attention has focused to date on the motion of spherical particles and there are several procedures available [10]. In the context of Stokes flows, Stokesian Dynamics [11,12],which is based on a truncated multipole expansion for the flow field, has been successful in the study of suspension mechanics and systems of particles. More generally for finite Reynolds number flows one of the available approaches for direct numerical simulation is the arbitrary Lagrangian–Eulerian formulation in conjunction with a finite element discretization, the so-called ALE scheme, see [13–15]. Here the numerical mesh conforms to the body geometry and evolves as the particles move with the flow. Other approaches include the distributed Lagrange multiplier (DLM) method and the lattice-Boltzmann method (LBM) [16,17]. DLM is a fictitious domain method based on virtual particles that does not rely on the movement of an underlying numerical mesh to resolve the motion of the particles, see [18,19]. LBM also employs a fixed computational grid and the influence of particles on the flow are interpolated back onto the grid.

* Corresponding author. Tel.: +1 401 863 1482; fax: +1 401 863 2722.
E-mail addresses: maxey@dam.brown.edu, Martin_Maxey@brown.edu (M.R. Maxey).

0021-9991/$ - see front matter © 2009 Elsevier Inc. All rights reserved.
doi:10.1016/j.jcp.2009.01.020

Another approach is the force-coupling method (FCM) developed by Maxey and Patel [20] and Lomholt and Maxey [21] for both low Reynolds number flow and finite Reynolds number flows, see [22]. FCM is also a fictitious domain method and relies on a low-order, finite force multipole expansion to represent the particles in the flow. The method has been compared successfully against experiments [23] and tested against direct numerical simulations [22,24] for a variety of conditions. FCM is computationally efficient and is able to accommodate large numbers of particles in fully three-dimensional flows, with a moderate $O(N_P)$ increase in effort beyond that needed for the underlying flow solver. While the method does not fully resolve the flow near each particle, it requires fewer grid points per particle than other schemes and provides reliable estimates for the particle motion. In the context of Stokes flow, FCM also captures the Faxén corrections to the drag force in non-uniform flows and the degenerate multipoles that are associated with the motion of rigid spherical particles.

The study of non-spherical particles, such as ellipsoids, has been more limited but is important for applications. Ellipsoids in Stokes flows are representative of short fibers or short chains of beads in suspension and their translational motion in a fluid is closely linked to their orientation [25]. Suspensions of ellipsoidal particles may spontaneously develop local inhomogeneities as they settle under gravity [26]. In a simple uniform shear flow, at low Reynolds numbers, ellipsoidal particles undergo a periodic rotation, giving the well-known Jeffery orbits [27]. An ellipsoidal particle settling under gravity in a non-uniform shear flow, however, may undergo a chaotic tumbling motion [28,29] due to the changes in settling motion with orientation.

Claeys and Brady [30] have extended Stokesian Dynamics to investigate the dynamics of spheroids in a Stokes suspension. Other studies of ellipsoidal particles in Stokes flow have generally been based on boundary integral formulations that resolve in detail the flow about each particle [31–34]. Studies involving elliptic (two-dimensional) particles in finite Reynolds number flows have been made using LBM [35,36] or with ALE schemes [37]. Qi and Luo [38] have applied LBM to the motion of three-dimensional spheroidal particles in Couette flow while Pan et al. [39] have extended DLM for the settling motion of an ellipsoid, and Swaminathan et al. [40] have similarly used ALE methods.

A number of other simulation methods have been developed for particles in suspension. The Physalis scheme [41] for rigid spherical particles relies on the existence of a local Stokes flow close to the particle surface, within some inner layer, that may be used to match boundary conditions to flow variables in an outer numerical simulation. Immersed boundary methods [42] have been developed for systems of rigid particles [43] and modified versions of DLM are available [44].

In this paper, we provide the extension of the force-coupling method for the motion of three-dimensional ellipsoidal particles. The method is derived first in the context of Stokes flow and compared with exact, analytical results for both open systems and channels. The method is then tested for several flows at finite Reynolds numbers and compared with direct numerical simulations. Of particular interest is the effect of wall boundaries on the motion. We also note the implementation of the scheme with the spectral/hp element method for computing the flow and the use of penalty methods for converting between resistance and mobility problems. Finally, some results are given for the tumbling motion of a pair of particles falling under gravity and for neutrally buoyant particles suspended in a shear flow.

2. FCM formulation

The force-coupling method [20,21] uses a set of finite force multipoles to represent the presence of each particle in the flow and fluid is assumed to fill the whole flow domain, including the volume occupied by the particles. The flow is specified in terms of a volumetric velocity field $\mathbf{u}(\mathbf{x},t)$ that is incompressible and satisfies

$$\rho\frac{D\mathbf{u}}{Dt} = -\nabla p + \mu\nabla^2\mathbf{u} + \mathbf{f}(\mathbf{x},t), \tag{1}$$

$$\nabla\cdot\mathbf{u} = 0, \tag{2}$$

where ρ, p and μ are the fluid density, pressure and viscosity, respectively. The source term $\mathbf{f}(\mathbf{x},t)$ represents the sum of two-way coupling forces from each particle n centered at $\mathbf{Y}^{(n)}(t)$. The source term for a single particle has the form:

$$f_i(\mathbf{x},t) = F_i\Delta(\mathbf{x}-\mathbf{Y}(t)) + G_{ij}\frac{\partial\Delta'(\mathbf{x}-\mathbf{Y}(t))}{\partial x_j}, \tag{3}$$

where $\Delta(\mathbf{x})$ and $\Delta'(\mathbf{x})$ are Gaussian distribution functions for the force monopole and dipole, respectively. For spherical particles the Gaussian envelope is isotropic in all directions and has the form

$$\Delta(\mathbf{x}) = (2\pi\sigma^2)^{-3/2}\exp[-\mathbf{x}^2/2\sigma^2], \tag{4}$$

where the length scale σ for the force monopole is related to the particle radius a by

$$a/\sigma = \sqrt{\pi}. \tag{5}$$

Similarly, the length scale σ' for the force dipole is given by

$$a/\sigma' = \left(6\sqrt{\pi}\right)^{1/3}. \tag{6}$$

The strength $\mathbf{F}$ of the finite force monopole in (3) is set by the sum of the external forces $\mathbf{F}^{ext}$, such as a magnetic force or force due to gravity, acting on the particle as well as the influence of inertia. If m_P is the mass of the particle and m_F is the mass of displaced fluid then, typically,

$$\mathbf{F} = \mathbf{F}^{ext} - (m_P - m_F)\frac{d\mathbf{V}}{dt}. \tag{7}$$

The second term in (3) is the force dipole of strength G_{ij}, which has symmetric and antisymmetric components. The symmetric, stresslet component of the force dipole G_{ij} is set so that

$$\int_D \frac{1}{2}\left(\frac{\partial u_i}{\partial x_j} + \frac{\partial u_j}{\partial x_i}\right)\Delta'(\mathbf{x} - \mathbf{Y})d^3\mathbf{x} = 0, \tag{8}$$

consistent with the constraint of rigid body motion. The antisymmetric component of the force dipole corresponds to a torque acting on the particle.

The velocity of each particle $\mathbf{V}(t)$ is evaluated from a volume integral of the fluid velocity using the monopole Gaussian distribution function as

$$\mathbf{V}(t) = \int_D \mathbf{u}(\mathbf{x}, t)\Delta(\mathbf{x} - \mathbf{Y}(t))d^3\mathbf{x}. \tag{9}$$

The angular velocity $\boldsymbol{\Omega}$ of the particle is computed by a corresponding volume average of the vorticity $\omega(\mathbf{x}, t)$ with the dipole Gaussian distribution function as

$$\boldsymbol{\Omega} = \frac{1}{2}\int_D \boldsymbol{\omega}(\mathbf{x}, t)\Delta'(\mathbf{x} - \mathbf{Y}(t))d^3x. \tag{10}$$

The new position of each particle is calculated from

$$\mathbf{V}(t) = \frac{d\mathbf{Y}(t)}{dt}. \tag{11}$$

The extension for ellipsoidal particles requires a generalization of the Gaussian envelope function (4) to account for the body shape. For an ellipsoid, centered at $\mathbf{Y} = 0$ with its principal axes aligned with the coordinate axes, the body surface is

$$\frac{x_1^2}{a_1^2} + \frac{x_2^2}{a_2^2} + \frac{x_3^2}{a_3^2} = 1. \tag{12}$$

The Gaussian envelope is then

$$\Delta(\mathbf{x}) = (2\pi)^{-3/2}(\sigma_1\sigma_2\sigma_3)^{-1}\exp\left[-\frac{1}{2}\left(\frac{x_1^2}{\sigma_1^2} + \frac{x_2^2}{\sigma_2^2} + \frac{x_3^2}{\sigma_3^2}\right)\right]. \tag{13}$$

As will be demonstrated, the length scale σ_k is related to the semi-axis a_k exactly as in (5) for the force monopole. The length scale σ_k' for the force dipole is similarly related to the semi-axis a_k exactly as in (6). In the limit of three equal semi-axes this matches the original formulation for the sphere (4).

The general orientation of an ellipsoid is specified by the orthogonal unit vectors $\mathbf{m}^{(1)}$, $\mathbf{m}^{(2)}$, $\mathbf{m}^{(3)}$ for the three principal semi-axes. These rotate with the rigid body as

$$\frac{d\mathbf{m}^{(k)}}{dt} = \boldsymbol{\Omega} \times \mathbf{m}^{(k)}. \tag{14}$$

The transformation between the fixed coordinate axes and the instantaneous semi-axes of an ellipsoid is specified by the orthogonal matrix Q with components $Q_{kn} = m_n^{(k)}$. The general form of the Gaussian envelope (13) is then

$$\Delta(\mathbf{x}) = (2\pi)^{-3/2}(\sigma_1\sigma_2\sigma_3)^{-1}\exp\left[-\frac{1}{2}\mathbf{x}^T Q^T \begin{pmatrix} \sigma_1^{-2} & 0 & 0 \\ 0 & \sigma_2^{-2} & 0 \\ 0 & 0 & \sigma_3^{-2} \end{pmatrix} Q\mathbf{x}\right]. \tag{15}$$

The remaining aspects of the force-coupling method remain unchanged. The particle velocity $\mathbf{V}$ and the angular velocity $\boldsymbol{\Omega}$ are evaluated by (9) and (10) as before, and the constraint (8) is used to determine the stresslet coefficient. We next consider the application of this reformulation for ellipsoidal particles to some canonical problems in Stokes flow to demonstrate that this provides the correct extension of the force-coupling method.

3. Isolated particle in stokes flow

In the context of low Reynolds number Stokes flow, it is possible to derive analytical results for the motion of an isolated spherical particle in an unbounded fluid domain. These results for both the flow and the resistance tensor, which relates the force and torque on the particle to $\mathbf{V}$ and $\boldsymbol{\Omega}$, may be compared directly with corresponding analytical solutions of the FCM equations [20,21]. These serve to validate FCM in the limit of a Stokes flow for isolated particles and to compare FCM results for the near-field and far-field flows with the exact closed form solutions. Closed, analytical results for the flow field past an ellipsoid are not available in any practical form. Theoretical results for the resistance tensor of a general ellipsoid are given by

Lamb [45] in terms of elliptic integrals and explicit results can be obtained for a prolate or oblate spheroid, see [46,47]. While the standard results are derived in a resistance format, the FCM results are obtained in a mobility formulation. We consider here the motion of a spheroid and compare the analytical results from FCM with the known, explicit closed form solutions and show that they are equivalent.

3.1. Settling of a spheroid

We consider first the motion of a particle in response to an applied force **F**. In general, the particle velocity is related to the force by the mobility tensor M as

$$V_i = M_{ij}F_j. \tag{16}$$

More commonly, the motion is specified in terms of a resistance tensor K with

$$F_i = K_{ij}V_j \tag{17}$$

and for an axisymmetric particle with the symmetry axis given by the unit vector **m** this has the form

$$K_{ij} = K_1 m_i m_j + K_2(\delta_{ij} - m_i m_j). \tag{18}$$

Explicit results for the resistance coefficient K_1 for motion parallel to the symmetry axis and K_2 for motion transverse to the axis are given by Happel and Brenner [46]. With $a_1 \geqslant a_2 = a_3$ and the aspect ratio $\lambda = a_1/a_2$, the resistance coefficients for a prolate spheroid are

$$\begin{aligned} K_1 &= 8\pi\mu a_2\tau^3[(2\tau^2+1)\log(\lambda+\tau) - \lambda\tau]^{-1}, \\ K_2 &= 16\pi\mu a_2\tau^3[(2\tau^2-1)\log(\lambda+\tau) + \lambda\tau]^{-1}, \end{aligned} \tag{19}$$

where $\tau^2 = |\lambda^2 - 1|$ and $\lambda \geqslant 1$. For an oblate spheroid with $\lambda \leqslant 1$ and $\tau^2 = |\lambda^2 - 1|$,

$$\begin{aligned} K_1 &= 8\pi\mu a_2\tau^3[(2\tau^2-1)\tan^{-1}(\tau/\lambda) + \lambda\tau]^{-1}, \\ K_2 &= 16\pi\mu a_2\tau^3[(2\tau^2-1)\tan^{-1}(\tau/\lambda) - \lambda\tau]^{-1}. \end{aligned} \tag{20}$$

The mobility tensor M for an ellipsoid can be evaluated from the force-coupling method. First the solution for the incompressible flow at zero Reynolds number can be found from (1) as a Fourier transform

$$\hat{u}_i = \frac{1}{\mu k^2}\left(\delta_{ij} - \frac{k_i k_j}{k^2}\right)\hat{f}_j, \tag{21}$$

where the Fourier transform is defined as

$$\hat{u}_i(\mathbf{k},t) = (2\pi)^{-3}\int u_i(\mathbf{x},t)\exp(-i\mathbf{k}\cdot\mathbf{x})d^3\mathbf{x} \tag{22}$$

and $k = |\mathbf{k}|$. The particle velocity **V** is found from the convolution integral (9) and for a particle centered at $\mathbf{Y} = 0$ the velocity is

$$V_i = (2\pi)^3\int \hat{u}_i(\mathbf{k},t)\widehat{\Delta}(\mathbf{k})d^3\mathbf{k}, \tag{23}$$

where $\widehat{\Delta}(\mathbf{k}) = (2\pi)^{-3}\exp\left\{-\left(k_1^2\sigma_1^2 + k_2^2\sigma_2^2 + k_3^2\sigma_3^2\right)/2\right\}$ when referred to the principal axes of the ellipsoid. The components of the mobility tensor are then

$$M_{ij} = \frac{1}{8\pi^3\mu}\int\left(\delta_{ij} - \frac{k_i k_j}{k^2}\right)\frac{1}{k^2}\exp\left\{-\left(k_1^2\sigma_1^2 + k_2^2\sigma_2^2 + k_3^2\sigma_3^2\right)\right\}d^3\mathbf{k}. \tag{24}$$

This is a diagonal matrix and is characterized by the settling velocity in response to a force applied separately in turn to each of the three principal axes. In each case, the velocity is then parallel to the force.

For an axisymmetric spheroid with the x_1-axis chosen to be the symmetry axis, the length scales σ_2 and σ_3 are equal and we set the ratio of the length scales as $\gamma = \sigma_1/\sigma_2$. The principal components M_{11} and $M_{22} = M_{33}$ can be evaluated by standard methods from (24) as

$$\begin{aligned} M_{11} &= (8\mu\pi^{3/2}\sigma_2)^{-1}\int_{-1}^{1}(1-t^2)\{1+(\gamma^2-1)t^2\}^{-1/2}\,dt, \\ M_{22} &= (16\mu\pi^{3/2}\sigma_2)^{-1}\int_{-1}^{1}(1+t^2)\{1+(\gamma^2-1)t^2\}^{-1/2}\,dt, \end{aligned} \tag{25}$$

where $t = k_1/k$. The values for a prolate spheroid, $\gamma > 1$, are

$$M_{11} = (8\mu\pi^{3/2}\sigma_2)^{-1}(\gamma^2-1)^{-3/2}\{(2\gamma^2-1)\log(\gamma+[\gamma^2-1]^{1/2}) - \gamma[\gamma^2-1]^{1/2}\},$$
$$M_{22} = (16\mu\pi^{3/2}\sigma_2)^{-1}(\gamma^2-1)^{-3/2}\{(2\gamma^2-3)\log(\gamma+[\gamma^2-1]^{1/2}) + \gamma[\gamma^2-1]^{1/2}\}. \tag{26}$$

These results (26) may be compared with the values of $1/K_1$ and $1/K_2$ from (19). The two sets of results are identical provided the coefficients for the aspect ratios are equal, $\gamma = \lambda$, and if $a_2 = \pi^{1/2}\sigma_2$ exactly as in (5). In particular, we see that for large aspect ratios λ there is the usual 2:1 ratio in the settling velocities.

There is also an identical match for oblate spheroids under the same conditions. The integrals in (25) can be evaluated using the change of variable $\sin z = t\sqrt{1-\gamma^2}$ for $\gamma < 1$ to obtain results identical to (20) with $M_{11} = 1/K_1$ and $M_{22} = 1/K_2$. Together these results confirm that the extended form of the Gaussian envelope (13) gives the appropriate generalization for the force monopole term.

3.2. Rotation of a spheroid

A spheroidal particle will rotate in response to an applied external torque, vorticity in the surrounding ambient flow or a local rate of strain in the ambient flow. This response is governed by the force dipole terms G_{ij}. If there is no rate of strain in the ambient flow and there is no external torque then no force dipole terms are induced and the particle rotates in response to the local vorticity as given by (10). If there is a rate of strain in the ambient flow then stresslet terms are induced and the particle rotates to align with the principal axes of the strain-rate. In a general shear flow there is a combination of these responses as seen in the well-known Jeffery orbits [27] for torque-free particles. The exact relation between the external torque $\mathbf{T}$, the angular velocity $\boldsymbol{\Omega}$ of the spheroid and the ambient flow is given by

$$T_i = \mu\left[R_1\left(\Omega_j - \frac{1}{2}\omega_j^\infty\right)m_j m_i + R_2\left(\left(\Omega_i - \frac{1}{2}\omega_i^\infty\right) - \left(\Omega_j - \frac{1}{2}\omega_j^\infty\right)m_j m_i\right)\right] - \mu R_2 D\epsilon_{ijk}m_j E_{kl}^\infty m_l, \tag{27}$$

where $D = (\lambda^2-1)/(\lambda^2+1)$, ω_i^∞ is the locally uniform vorticity, and E_{ij}^∞ is the locally uniform rate of strain. For a prolate spheroid

$$R_1 = \frac{16}{3}\pi a_2^3\tau^3[\lambda\tau - \log(\lambda+\tau)]^{-1},$$
$$R_2 = \frac{16}{3}\pi a_2^3\tau^3(1+\lambda^2)[(2\tau^2+1)\log(\lambda+\tau) - \lambda\tau]^{-1} \tag{28}$$

with, as before, the aspect ratio $\lambda > 1$, $\tau^2 = |\lambda^2 - 1|$ and a_2 the radius perpendicular to the axis of symmetry $\mathbf{m}$. For an oblate spheroid, $\lambda < 1$,

$$R_1 = \frac{16}{3}\pi a_2^3\tau^3[\tan^{-1}(\tau/\lambda) - \lambda\tau]^{-1},$$
$$R_2 = \frac{16}{3}\pi a_2^3\tau^3(1+\lambda^2)[(2\tau^2-1)\tan^{-1}(\tau/\lambda) + \lambda\tau]^{-1}, \tag{29}$$

see [46].

When using the force-coupling method, the key step is to evaluate the velocity gradient averaged over the particle

$$\Gamma_{ij} = \int \frac{\partial u_i}{\partial x_j}\Delta'(\mathbf{x}-\mathbf{Y})d^3\mathbf{x} \tag{30}$$

for the flow $\mathbf{u}(\mathbf{x},\mathbf{t})$ induced by the force dipole terms G_{ij}. The angular velocity is then determined (10) as

$$\Omega_i = \frac{1}{2}\omega_i^\infty + \frac{1}{2}\epsilon_{ijk}\Gamma_{kj}. \tag{31}$$

In Stokes flow, the external torque $\mathbf{T}$ determines the antisymmetric terms of the force dipole as $G_{ij}^A = \frac{1}{2}\epsilon_{ijk}T_k$. The symmetric stresslet components G_{ij}^S are set so as to ensure that the net rate of strain averaged over the particle is zero (8),

$$\frac{1}{2}(\Gamma_{ij} + \Gamma_{ji}) + E_{ij}^\infty = 0. \tag{32}$$

The 'mobility' relation between Γ_{ij} and G_{ij} is found in the same manner as before from the Fourier transform of the flow (21) and is

$$\Gamma_{ij} = A_{ipjq}G_{pq}, \tag{33}$$

where

$$A_{ijkm} = -\frac{1}{8\pi^3\mu}\int\left(\delta_{ij} - \frac{k_i k_j}{k^2}\right)\frac{k_k k_m}{k^2}\exp\left\{-\left[k_1^2\sigma_1'^2 + \left(k_2^2+k_3^2\right)\sigma_2'^2\right]\right\}d^3\mathbf{k}. \tag{34}$$

The symmetry axis $\mathbf{m}$ has been taken be parallel to the x_1-axis and the components are referred the principal axes of the spheroid. We will assume that the ratio σ_1'/σ_2' matches the aspect ratio λ and that a_2 and σ_2' are related as in (6). We will then demonstrate that the results obtained for three canonical cases match the known exact results.

In general A_{ijkm} is an axisymmetric tensor. Further, from (34), the tensor A_{ijkm} is symmetric with respect to the index pair $i,\ j$ and with respect to $k,\ m$. The tensor then has the general form

$$A_{ijkm} = \alpha_1\delta_{ij}\delta_{km} + \alpha_2(\delta_{ik}\delta_{jm} + \delta_{im}\delta_{jk}) + \alpha_3\delta_{ij}m_km_m + \alpha_4(\delta_{ik}m_jm_m + \delta_{im}m_jm_k + \delta_{jk}m_im_m + \delta_{jm}m_im_k) + \alpha_5\delta_{km}m_im_j + \alpha_6m_im_jm_km_m. \tag{35}$$

The coefficients are further restricted by the incompressibility condition that $A_{ijim} = 0$. These give

$$\begin{aligned} &\alpha_1 + 4\alpha_2 + \alpha_4 = 0,\\ &\alpha_3 + 5\alpha_4 + \alpha_5 + \alpha_6 = 0. \end{aligned} \tag{36}$$

This ensures too that $A_{ijkj} = 0$ and that the trace of the stresslet has no effect on the particle motion. There are then four independent coefficients that determine A_{ijkm}. The details of their evaluation are given in the Appendix.

The first example is the rotation of a spheroid about the axis of symmetry, with no ambient flow, under the action of an external torque $T_1\mathbf{m}$. The angular velocity is $\Omega_1\mathbf{m}$ and for this axisymmetric motion there is no induced stresslet G^S_{ij} as (32) is directly satisfied. Here,

$$\begin{aligned} \Gamma_{23} &= \alpha_1G_{23} + \alpha_2G_{32},\\ \Gamma_{32} &= \alpha_2G_{23} + \alpha_1G_{32}, \end{aligned} \tag{37}$$

and from (31)

$$\Omega_1 = \frac{1}{2}(\Gamma_{32} - \Gamma_{23}). \tag{38}$$

The torque $T_i = \epsilon_{ijk}G_{jk}$ and here $G_{23} = -G_{32} = \frac{1}{2}T_1$. The angular velocity Ω_1 is then related to the torque T_1 by

$$\Omega_1 = \frac{1}{2}(\alpha_2 - \alpha_1)T_1. \tag{39}$$

Using the notation from the Appendix, $(\alpha_2 - \alpha_1) = C(I_0 - I_1)$ from (A.9) and for a prolate spheroid with $\lambda > 1$,

$$\Omega_1/T_1 = \frac{3}{16\pi\mu a_2^3}\frac{1}{\tau^3}(\lambda\tau - \log(\lambda + \tau)). \tag{40}$$

For an oblate spheroid, $\lambda < 1$,

$$\Omega_1/T_1 = \frac{3}{16\pi\mu a_2^3}\frac{1}{\tau^3}(\tan^{-1}(\tau/\lambda) - \lambda\tau). \tag{41}$$

These results exactly match the results for $(\mu R_1)^{-1}$ in (28) and (29).

In the next example, rotation about an axis orthogonal to the symmetry axis under an external torque induces a stresslet response. With $\mathbf{m}$ aligned with the x_1-axis, a torque applied parallel to the x_2-axis will lead to dipole terms G_{13} and G_{31} giving

$$\begin{aligned} \Gamma_{13} &= b_3G_{13} + b_6G_{31},\\ \Gamma_{31} &= b_6G_{13} + b_4G_{31}, \end{aligned} \tag{42}$$

in terms of the coefficients (A.1) from the Appendix. The condition (32) gives

$$G_{13} = -(b_4 + b_6)G_{31}/(b_3 + b_6) \tag{43}$$

and the torque, which is $T_2 = G_{31} - G_{13}$ is then

$$T_2 = \left[1 + \frac{b_4 + b_6}{b_3 + b_6}\right]G_{31}. \tag{44}$$

The angular velocity $\Omega_2 = (\Gamma_{31} - \Gamma_{13})/2$ is

$$\Omega_2 = \frac{b_6^2 - b_3b_4}{b_3 + b_6}G_{31} \tag{45}$$

and so the torque and angular velocity are related as

$$\Omega_2 = \frac{b_6^2 - b_3b_4}{b_3 + b_4 + 2b_6}T_2. \tag{46}$$

This relation is evaluated from (A.5) using the results for the integrals (A.6) and (A.7). For a prolate spheroid, $\lambda > 1$,

$$\Omega_2/T_2 = \frac{3}{32\pi\mu a_2^3}\left(\frac{(2\tau^2 + 1)I_1 + I_0}{\lambda^2 + 1}\right) = \frac{3}{16\pi\mu a_2^3}\frac{(2\tau^2 + 1)\log(\lambda + \tau) - \lambda\tau}{\tau^3(\lambda^2 + 1)}, \tag{47}$$

while for an oblate spheroid, $\lambda < 1$,

$$\Omega_2/T_2 = \frac{3}{32\pi\mu a_2^3}\left(\frac{I_0-(2\tau^2-1)I_1}{\lambda^2+1}\right) = \frac{3}{16\pi\mu a_2^3}\frac{(2\tau^2-1)\tan^{-1}(\tau/\lambda)+\lambda\tau}{\tau^3(\lambda^2+1)}. \tag{48}$$

These results exactly match the results for $(\mu R_2)^{-1}$ in (28) and (29).

The stresslet term $G_{13}^S = (G_{13}+G_{31})/2$ is related to the angular velocity by

$$G_{13}^S = \frac{b_3-b_4}{2\left(b_6^2-b_3b_4\right)}\Omega_2. \tag{49}$$

When evaluated, this expression also exactly matches the values given by Kim and Karrila [47].

The last example is the torque required to hold a particle fixed when placed in a pure straining flow. For this case, we again align the axis of symmetry with the x_1-direction, and the principal axes for the locally uniform rate of strain are in the x_1, x_3-plane, making an angle of 45° to the x_1-axis. The non-zero components of the rate of strain are E_{13}^∞ and E_{31}^∞ which tend to turn the particle to align with the principal axes. We consider the torque in the x_2-direction needed to keep the particle in place without rotation. Therefore, from (31) and (32),

$$\begin{aligned} 0 &= \frac{1}{2}(\widetilde{\Gamma}_{31}-\widetilde{\Gamma}_{13}),\\ E_{13}^\infty &= -\frac{1}{2}(\widetilde{\Gamma}_{13}+\widetilde{\Gamma}_{31}). \end{aligned} \tag{50}$$

As in the previous example there are just two non-zero components of the force dipole G_{13} and G_{31}, which again satisfy (42). From (50) it follows that

$$G_{13} = \frac{b_4-b_6}{b_3-b_6}G_{31}, \tag{51}$$

which then implies

$$T_2 = \frac{b_3-b_4}{b_3-b_6}G_{31}. \tag{52}$$

In terms of the imposed rate of strain,

$$E_{13}^\infty = \frac{b_6^2-b_3b_4}{b_3-b_6}G_{31} = \frac{b_6^2-b_3b_4}{b_3-b_4}T_2. \tag{53}$$

For a prolate spheroid,

$$\frac{b_6^2-b_3b_4}{b_3-b_4} = \frac{1}{2}\frac{3}{16\pi\mu a_2^3}\left(\frac{(2\tau^2+1)I_1+I_0}{\tau^2}\right) = \frac{3}{16\pi\mu a_2^3}\frac{1}{\tau^5}((2\tau^2+1)\log(\lambda+\tau)-\lambda\tau) \tag{54}$$

and for an oblate spheroid

$$\frac{b_6^2-b_3b_4}{b_3-b_4} = \frac{1}{2}\frac{3}{16\pi\mu a_2^3}\left(\frac{(2\tau^2-1)I_1-I_0}{\tau^2}\right) = \frac{3}{16\pi\mu a_2^3}\frac{1}{\tau^3(\lambda^2-1)}((2\tau^2-1)\tan^{-1}(\tau/\lambda)+\lambda\tau). \tag{55}$$

Again, these FCM results exactly match the corresponding expression in (27) and reduce to $(\mu R_2 D)^{-1}$ as given by (28) and (29).

3.3. Faxén terms

The external force required to hold a spherical particle of radius a fixed in a nonuniform Stokes flow $\mathbf{u}^\infty(\mathbf{x})$ is given by Faxén's first law as

$$\mathbf{F} = -6\pi\mu a\left(\mathbf{u}^\infty+\frac{1}{6}a^2\nabla^2\mathbf{u}^\infty\right)_o, \tag{56}$$

where subscript o indicates evaluation at the particle center, see [48]. This result given in resistance form may be rewritten as a modified mobility relation so that the velocity of a sphere subject to an external force $\mathbf{F}$ in the presence of an ambient Stokes flow $\mathbf{u}^\infty$ is

$$\mathbf{V} = \frac{1}{6\pi\mu a}\mathbf{F}+\left(\mathbf{u}^\infty+\frac{1}{6}a^2\nabla^2\mathbf{u}^\infty\right)_o. \tag{57}$$

This feature is captured by FCM through (9) to a good approximation, within 5% [20]. The exact coefficient in (57) is $a^2/6$ as compared to $\sigma^2/2$ from FCM. Similarly, Faxén's second law for the angular velocity and torque on a sphere in a nonuniform flow is obtained directly from (10).

Brenner [49,46] extended Faxén's laws to ellipsoidal particles and this result may be expressed from (16) as a mobility relation

$$V_i = M_{ij}F_j + \left(u_i^\infty + \frac{1}{3!}D^2u_i^\infty + \frac{1}{5!}D^4u_i^\infty + \cdots\right)_o, \tag{58}$$

where the operator D^2 is defined as

$$D^2 = a_1^2\frac{\partial^2}{\partial x_1^2} + a_2^2\frac{\partial^2}{\partial x_2^2} + a_3^2\frac{\partial^2}{\partial x_3^2}. \tag{59}$$

The rescaling for the three principal axes in (59) of D^2 relative to $a^2\nabla^2$ is consistent with the definition of the envelope (13) for the ellipsoid. This result (59) may be compared to the corresponding results from (9) for FCM, obtained by substituting an appropriate Taylor series expansion for $\mathbf{u}^\infty$. The first correction term involving $D^2\mathbf{u}^\infty$ is approximated to within 5% as before by FCM. The coefficient of 1/6 in (58) is $1/(2\pi)$ in the FCM result. While FCM gives the correct functional form of (58), FCM fails to match the coefficients of the additional higher order derivative terms. The Faxén corrections are derived on the assumption that the ambient flow is slowly varying, on a length scale L, large compared to the particle dimension [46]. As a result these higher order derivatives should be less significant.

The Faxén relation for the angular velocity and torque in the presence of an ambient flow is similarly modified. Following [48], the leading correction term is $\frac{1}{10}(D^2\boldsymbol{\omega}^\infty)_o$. The corresponding result from (10) for FCM gives a coefficient of $\frac{1}{2}(36\pi)^{-1/3}$ instead of the exact value $\frac{1}{10}$, but matches to within 4% and has the correct functional form. Again, FCM fails to match the coefficients of the terms involving higher order derivatives.

4. Simulation method

Where particles are suspended in a low Reynolds number flow with a confining geometry or in a flow at finite Reynolds number it is necessary to combine the force-coupling method with a numerical flow solver. Here FCM is implemented with the *NEKTAR* code, a three-dimensional spectral/hp element solver for incompressible flow [50]. The solutions to the equations of motion for the flow (1) and (2) are computed with the presence of the particles represented by the body force distribution (3). The implementation is similar to that for spherical particles [22]. Modified Jacobi polynomials form the basis functions for the spectral elements and standard finite element hybrid meshes are used to match the fixed geometry of the flow domain. The spatial resolution may be controlled by varying the order of the polynomials or refining the finite element mesh. An explicit, stiffly stable time-splitting scheme is used to ensure incompressibility of the flow field and the resulting Poisson equation for the pressure field is obtained using a preconditioned conjugate gradient method. Further details are given by Liu [24].

The velocity of a freely moving particle is obtained from (9) and the particle position $\mathbf{Y}(t)$ computed from (11) using the same time-stepping scheme. In addition, for the ellipsoidal particles in three-dimensions, the particle angular velocity is computed from (10) and the principal axes of the body computed from (14). Some simplifications are possible if the motion of the particle is confined to a plane and then only an orientation angle needs to be specified.

In the following section, we compare the computational results obtained with FCM for particles fixed in the flow, or moving with a prescribed velocity, with corresponding results from fully resolved, direct numerical simulations (DNS). These latter simulations are also computed with *NEKTAR* but with a higher resolution and impose the exact boundary conditions on the particle surface. A frame of reference is used in which the particle is fixed and the mesh is fitted to both the particle geometry and the flow domain. In the simulations with FCM, the spatial resolution needed is dictated by the need to accurately represent the force distribution (3). On a uniform grid, using a high-order method such as Fourier pseudo-spectral representation, the ratio of the smallest value of σ' should exceed Δx, the grid spacing. Good results are obtained if $\sigma' = 1.25\Delta x$, which gives an estimate of 5.5 points to the shortest particle diameter. With just the force monopole term, $\sigma = \Delta x$ gives acceptable results and corresponds to 3.5 grid points to the shortest major axis. This is the coarsest possible resolution and results degrade quickly below this. For a spectral element representation, where the mesh is nonuniform and a particle may be located anywhere in the mesh, the estimate of Δx should be based on the largest spacing between collocation points within an element.

The force-coupling method is formulated as a mobility problem, where the forces and torques on the particles are prescribed and the particle velocities are then evaluated. This is in contrast to the DNS results that are obtained from a resistance problem, where the velocities are specified and the forces evaluated from the simulations. In order to compare the two, a *penalty scheme* is used with FCM to simulate resistance problems. For example, to calculate the external force $\mathbf{F}$ and torque $\mathbf{T}$ required to hold a particle fixed in a flow driven by a pressure gradient, a set of simple differential equations are formulated relating the force monopole term and antisymmetric components of the force dipole in (3) to the instantaneous particle velocity $\mathbf{V}$ and angular velocity $\boldsymbol{\Omega}$. These equations are

$$\frac{d\mathbf{F}(t)}{dt} = -\lambda_1\mathbf{V}(t), \tag{60}$$

$$\frac{d\mathbf{T}(t)}{dt} = -\lambda_2\boldsymbol{\Omega}(t). \tag{61}$$

The antisymmetric components of the force dipole are then given as

$$G_{ij} - G_{ji} = \epsilon_{ijk} T_k. \tag{62}$$

Here λ_1 and λ_2 are the dimensional penalty parameters. Their magnitude controls the speed of convergence; the larger they are the faster the convergence. However, for stability reasons, they cannot be too large. Upon convergence to a steady state where $\mathbf{V} = 0$ and $\mathbf{\Omega} = 0$, $\mathbf{F}(t)$ and $\mathbf{T}(t)$ become independent of time t, and the required force and torque are therefore obtained. A third-order, Adams–Bashforth method is used to discretize the above equations.

The penalty scheme may be used for simple steady motion, in which case the equations are evolved over time until a steady state is achieved. Alternatively, in a flow that is developing over time, the penalty scheme may be used as an inner "pseudo-time-stepping" scheme, applied for each time-step of the flow, until a converged state is reached. During the course of this inner time-step, there is no change in the particle position or orientation.

A similar penalty method may be used, either directly or as an inner time-stepping procedure, to obtain the symmetric (stresslet) components of the force dipole $G_{ij}^{(S)}$. The convergence condition is that the strain-rate $\widetilde{E}_{ij}^k$ for each particle k,

$$\widetilde{E}_{ij}^k = \int_D \frac{1}{2}\left(\frac{\partial u_i}{\partial x_j} + \frac{\partial u_j}{\partial x_i}\right) \Delta'(\mathbf{x} - \mathbf{Y}^k) d^3x, \tag{63}$$

satisfies a condition on the L_2 norm and that $\|\widetilde{E}_{ij}^k\| \leqslant \epsilon$ for some specified tolerance ϵ. The differential equation for the penalty scheme in this case may be written as

$$\frac{dG_{ij}^{(S)k}}{dt} = \lambda_3 \widetilde{E}_{ij}^k, \tag{64}$$

where λ_3 is the dimensional penalty coefficient. As is evident from (27), the torque on an ellipsoidal particle depends on both the angular velocity and the rate of strain in the flow. Penalty methods for the torque and stresslet components of the force dipole should be applied concurrently.

Where the external torque on the particle is known, for example for a freely moving particle with no external torque acting on it, an alternative iterative procedure may be used to set the symmetric force dipole at each time level. The procedure is described in Dance and Maxey [51] for the context of spherical particles in a Stokes flows. In summary, the flow is advanced to an intermediate time level as $\mathbf{u}'$, p' using the equations of motion (1)–(3) and the standard *NEKTAR* scheme. The previous values of $G_{ij}^{(S)k}$ are used to do this. From this intermediate flow the strain-rate $\widetilde{E}_{ij}^k$ for each particle is evaluated and based on this a first correction to the force dipole is estimated as

$$dG_{ij}^k = \frac{20}{3}\pi a_i^3 \mu \widetilde{E}_{ij}^k, \tag{65}$$

where a_i is the intermediate semi-axis of the particle. Then we solve the following Stokes problem for the perturbation velocity u_i^*:

$$\rho \frac{\partial u_i^*}{\partial t} = -\frac{\partial p^*}{\partial x_i} + \mu \frac{\partial^2 u_i^*}{\partial x_i^2} + \sum_{k=1}^{N} dG_{ij}^k \frac{\partial \Delta'(\mathbf{x} - \mathbf{Y}^k)}{\partial x_j}. \tag{66}$$

We use Eq. (63) to compute $\widetilde{E}_{ij}^{k*}$, the strain-rate from the perturbation velocity u_i^*. In essence, we use these results to recalibrate the estimate (65) assuming that the change in strain-rate for a particle is dominated by the stresslet applied to that particle. For each particle, a coefficient λ_k is determined so as to minimize $\|\widetilde{E}_{ij}^k + \lambda_k \widetilde{E}_{ij}^{k*}\|$. The dipole term for particle k is then rescaled and updated as

$$G_{ij}^k + \lambda_k dG_{ij}^k \Rightarrow G_{ij}^k. \tag{67}$$

This new estimate for the force dipole is then used and the iteration repeated until the norm of the particle strain-rate is below the specified tolerance threshold.

5. Prescribed particle motion

In this section, we consider the flow field and fluid forces associated with a single ellipsoidal particle held fixed in a shear flow or moving with a prescribed constant velocity in otherwise still fluid. We compare the results of FCM simulations with corresponding fully resolved, direct numerical simulations (DNS) to determine the relative accuracy of FCM in calculating the particle forces or the disturbance flows. Past experience from simulations of spherical particles is that particle forces and velocities can be determined with good accuracy and that the flow away from the immediate region surrounding the particle is well resolved [21,22]. The flow structure close to the particle is smoothed by the effective spatial filter of the force envelope (13). The results in this section, for both Stokes flow and finite Reynolds number flow, show the same general features.

In the computations, values are assigned to the fluid parameters so that the density $\rho = 1$ and the dynamic viscosity $\mu = 1$. We adopt a reference length scale, $a = 1$, representative of the particle size and all length scales are specified in terms of a.

5.1. Settling in a vertical duct

The first example is of an ellipsoidal particle settling in a vertical channel or duct, where the horizontal cross-section is a square with rigid side-walls located at $x_2/a = \pm 3.5$ and $x_3/a = \pm 3.5$. No-slip boundary conditions are applied on the fixed side-walls while a periodic boundary condition is applied in the vertical direction for the domain $0 \leqslant x_1/a \leqslant 16$. The ellipsoid has principal semi-axes $a_1 = 1.5a,\ a_2 = 0.9a$ and $a_3 = 1.2a$. These symmetry axes of the particle are fixed and aligned with the corresponding coordinate axes for the channel. The particle settles under a constant force due to gravity along the centerline of the duct. The particle is placed initially at $x_1/a = 7,\ x_2/a = 0$ and $x_3/a = 0$ and falls in the negative x_1-direction.

In the FCM simulations, a simple uniform mesh of 256 hexahedral elements is used, consisting of 16 elements in the x_1-direction and four elements in both the x_2 and x_3 directions. The basis functions within each spectral element consist of modified Jacobi polynomials of degree 11. This ensures that the conditions on spatial resolution for a particle in FCM are met. A constant external force F_1 is applied to the particle and to the fluid (7) and the velocity V_1 determined from (9) based on the computed flow field.

The results from DNS are obtained with a more refined mesh of 10,240 hexahedral elements. The elements accurately represent the geometry of the ellipsoid and the duct. A fourth-order polynomial expansion is used within each spectral element. In order to allow for the use of a fixed mesh, the simulations are done in a frame of reference in which the particle is fixed but the side-walls of the channel move upwards at a constant velocity. This velocity is set from the final result of the FCM simulations and the flow from the DNS is used to compute the fluid force on the particle. We, thus, compare the forces on the particle required to achieve a specific settling velocity.

We consider first the results for a Stokes flow. The FCM results are obtained with the *NEKTAR* code, used as a solver for unsteady Stokes flow and the nonlinear inertial terms in (1) are omitted. Even though the particle velocity is computed, the particle position (11) is not updated so as to ensure a consistent neglect of inertial effects. The magnitude of the applied force is 6π and for an isolated sphere of radius $a = 1$ in open fluid this would result here in a terminal fall speed $V_1 = 1.0$. (For convenience we consider F_1 and V_1 as positive quantities although both are negative.) The converged value for the settling velocity of the ellipsoid is $V_1 = 0.5481$. This is used to set the upward velocity of the side-walls in the DNS. The *NEKTAR* code is again used as a solver for unsteady Stokes flow. An implicit backward Euler scheme is used for the viscous terms permitting larger time steps and a more rapid convergence to the final steady flow. DNS gives the value $F_1 = 18.76$. In nondimensional form, the force on the particle $F_1/(\mu a V_1)$ is equal to 34.390 from FCM and 34.235 from DNS, which represents a difference of 0.5% and is within the range of error for the numerical computations.

Fig. 1 shows the profiles for the fluid velocity components u_1 and u_2 as a function of x_2. These profiles are taken at different streamwise locations x_1/a in the plane $x_3 = 0$. The results of FCM are compared to DNS and we use the frame of reference of the DNS where the particle is fixed and side-walls are moving. At $x_1/a = 7$, passing through the particle center, the FCM results agree well with DNS outside the region $\pm 1.5a_2$. At $x_1/a = 8.5$, tangential to particle surface, and at $x_1/a = 10$, a distance of a_1 from the surface, there is good agreement between the computed profiles for the Stokes flow.

The corresponding vorticity profiles are shown in Fig. 2, where the vorticity component ω_3 is shown versus x_2 in the symmetry plane $x_3 = 0$ and the vorticity component ω_2 versus x_3 is given for the plane $x_2 = 0$. The different streamwise locations are the same as in Fig. 1. Along the diameters passing through the particle center, $x_1/a = 7$, the FCM simulations underestimate the vorticity in the flow near to the particle surface. The results of DNS show that the peak values of vorticity occur at the surface and then drop sharply to zero inside the particle volume. FCM, on the other hand, gives a smooth transition

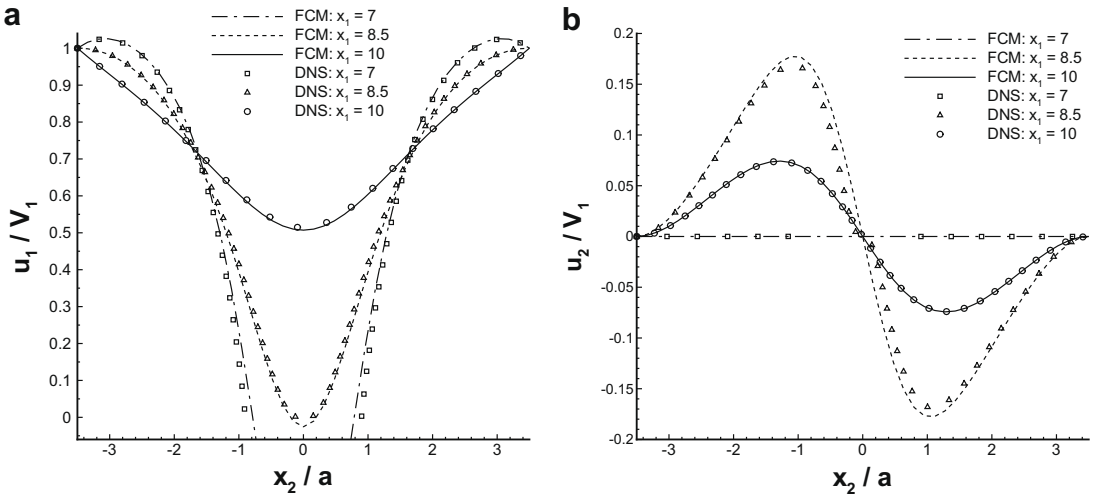

Fig. 1. Fluid velocity profiles in x_2 across the duct for settling ellipsoid, aligned vertically in Stokes flow. Velocities are relative to the particle: (a) u_1; (b) u_2. Legend gives streamwise location, relative to center at $x_1/a = 7$, comparing DNS and FCM results.

within the particle volume, which for FCM is an active part of the flow domain and must be accounted for in evaluating viscous dissipation and other physical quantities [20]. Similar features are seen at $x_1/a = 8.5$, near to the tip of the ellipsoid, while at $x_1/a = 10$ there is full agreement between DNS and FCM.

The settling of the particle at finite Reynolds numbers may be evaluated with the same procedures, using the full *NEKTAR* code. The same meshes and spectral elements are used as for the Stokes flow. A constant force is applied in the FCM simulations and the particle velocity evaluated. This velocity is then used to set the velocity of the side-walls in the DNS for motion relative to a fixed particle. In a mobility problem, typical of sedimentation, the usual Reynolds number based on particle velocity is a derived quantity. Alternatively, a Reynolds based on the applied force may be specified directly as $Re_F = F/\mu\nu$, where $\nu = \mu/\rho$ is the kinematic viscosity. In the present example, $Re_F = 180.6$ and for an isolated sphere of radius a settling in otherwise still fluid this would correspond to a particle Reynolds number $Re = 2aV/\nu$ of 10.0. The FCM simulations give $V_1 = -4.995$ and the particle Reynolds number based on the smallest semi-axis a_2, $Re = 2a_2V/\nu$ has a value of 8.99. The nondimensional force on the particle, $F_1/(\mu a V_1)$, is equal to 36.157 from FCM and 35.768 from DNS, which represents a difference of 1.1%

Fig. 3 shows the profiles for fluid velocity components u_1 and u_2 as a function of x_2 in the plane $x_3 = 0$ for the frame of reference in which the particle is fixed. These profiles are taken at different streamwise x_1 locations at the particle center, tangential to the particle tips in both the wake and ahead of particle, and at distances $2a_1$ from the center in both wake and ahead of particle. At the particle center, along the diameter, the FCM and DNS profiles match outside the region $x_2 = \pm 1.5a_2$. At the two ends of the ellipsoid there is generally good agreement in the profiles. At the tip, on the leading side, the profiles match but there is a more noticeable difference in the wake at the tip.

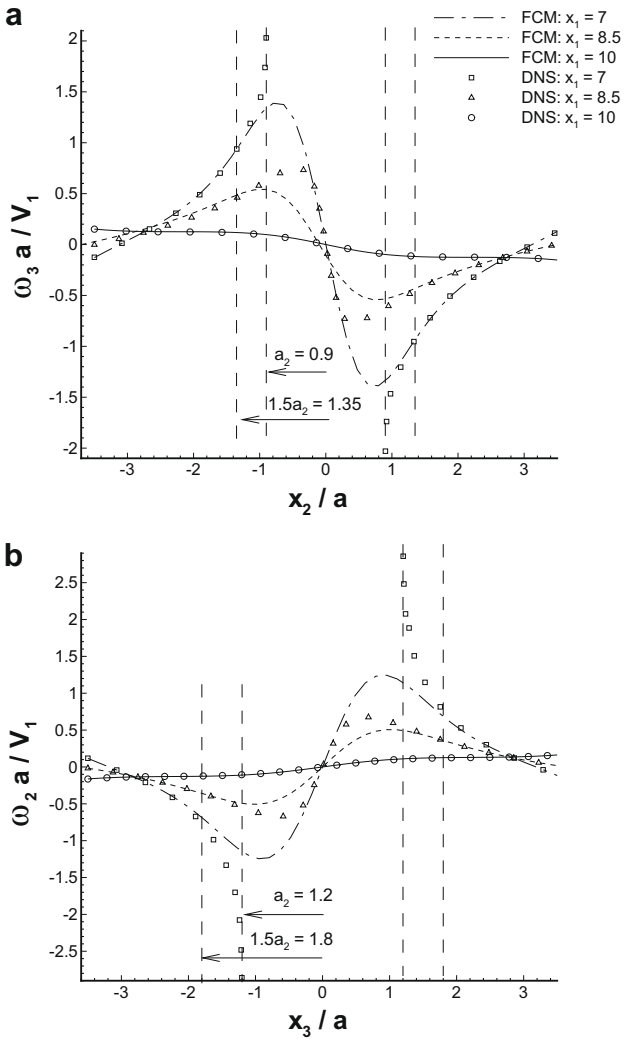

Fig. 2. Vorticity profiles for settling ellipsoid in Stokes flow: (a) ω_3 versus x_2; (b) ω_2 versus x_3. Legend gives streamwise location, relative to center at $x_1/a = 7$, comparing DNS and FCM results.

It should be noted that this orientation for an ellipsoid settling under gravity is unstable at finite Reynolds number. As illustrated in Section 6, an ellipsoid will turn to fall broadside on.

5.2. Spheroid aligned in a Poiseuille flow

The second example is for a spheroidal particle, held at a fixed position near a wall, in a Poiseuille flow between two parallel plane walls. The spheroid has semi-axes $a_1/a = 2,\ a_2/a = a_3/a = 1$ and the symmetry axis of the particle is aligned with the streamwise x_1-direction of the flow. This corresponds to an example given by Happel and Brenner [46] for a spheroidal particle in Stokes flow and for which analytical results for the drag force are available. The flow configuration is illustrated in Fig. 4. The particle is placed midway between the lower channel wall and the centerline of the channel. The particle center is used as the origin for the coordinate axes and the channel walls are located at $x_2/a_2 = -3.333$ and $x_2/a_2 = 10.0$. No-slip conditions are applied on the walls and periodic boundary conditions are applied in the spanwise direction for the region $-L_3 \leqslant x_3 \leqslant L_3$.

A parabolic velocity profile is generated by a pressure gradient applied to the flow and in the absence of a particle, the fluid velocity is

$$u_1 = u_o(1 + 0.3x_2/a_2)(1 - 0.1x_2/a_2). \tag{68}$$

The reference velocity u_o is the approach velocity or the fluid velocity of the undisturbed flow at the location of the particle. The centerline velocity for this flow is $u_{cl} = 1.333u_o$.

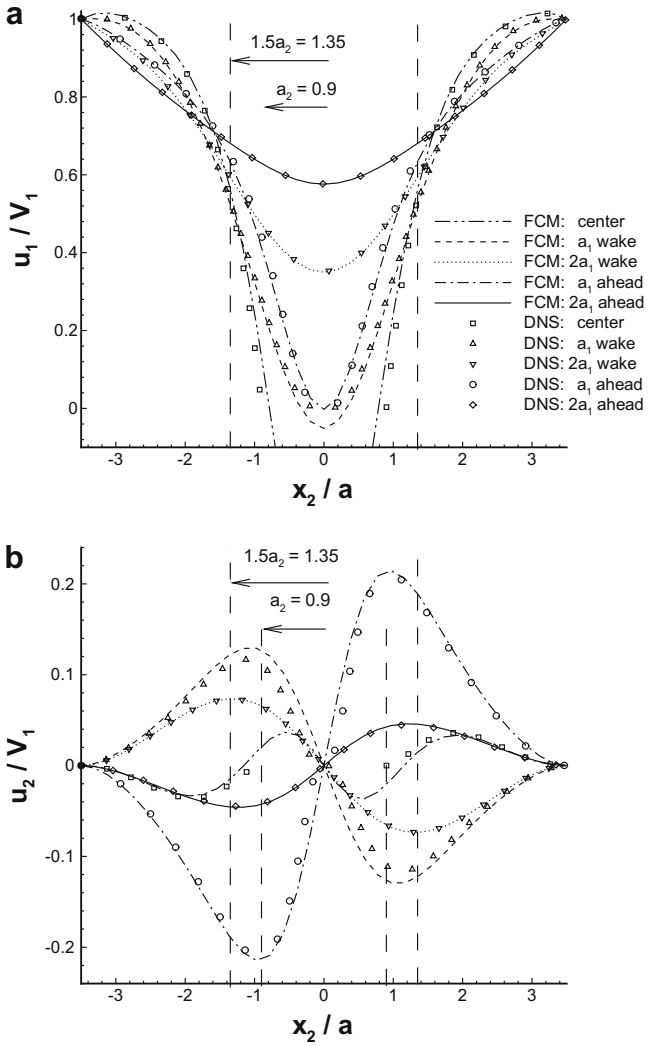

Fig. 3. Fluid velocity profiles in x_2 across the duct for settling ellipsoid, aligned vertically, at $Re_F = 181$. Velocities are relative to the particle: (a) u_1; (b) u_2. Legend gives streamwise location, relative to the particle's center, comparing DNS and FCM results.

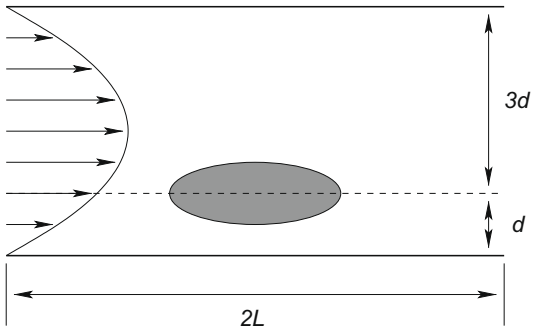

Fig. 4. Schematic sketch of spheroid held fixed at $\mathbf{x} = 0$ in a Poiseuille flow in a channel. Spheroid is midway between lower wall, $x_2 = -d$ and centerline of the channel, $x_2 = d$, with axis aligned with primary shear flow $u_1(x_2)$. Periodic boundary conditions are applied in x_3-direction at $x_3 = \pm L_3$ and in x_1-direction at $x_1 = \pm L$; $d = 10a/3$.

We first summarize the results for a Stokes flow. In order to compare with the results of Happel and Brenner [46], the channel walls should approximate infinite plane boundaries. The results given here are based on $L_3/a_2 = 20$ and for a periodic domain $-80 \leqslant x_1/a_2 \leqslant 80$. The simulations using FCM are computed for a structured mesh of 2400 hexahedral elements. There are 20 elements in the x_1 direction, with much smaller elements in the middle $x_1 = 0$; 20 elements in the x_2 direction, with smaller elements nearer the wall at $x_2 = -3.3333$; and six elements in the x_3 direction, again with smaller elements in the middle $x_3 = 0$. The penalty method is applied to keep the particle fixed and to find the restoring force and torque from Eqs. (60) and (61).

Once converged, the particle velocity and angular velocity are reduced to negligible levels. The results for the nondimensional drag force $F_1/(\mu a_2 u_o)$ and torque on the particle are given in Table 1. There is no lift force F_2 on the particle because of the symmetry of the Stokes flow and none is generated in the FCM simulation. When compared to an isolated spheroid held fixed in a uniform flow $\mathbf{u} = (u_o, 0, 0)$, the results from the Table 7–5.1 in [46] show that the fluid drag force should be 27% greater in the channel flow. A comparison of the results in Table 1 shows that the FCM result for F_1 matches the theoretical result within 1.5%. The computational errors in the flow field and the force estimates are in the range of 0.5–1%, as determined by comparison with a further simulation with a similar but slightly different element mesh. The size of the periodic domain will also affect the comparison. Reducing L_3 to $L_3/a_2 = 10$ in the spanwise direction increases the estimated drag force by about 5%. Tests indicate that with the chosen periodic domain the effect of domain size on the computed drag force is no larger than the other sources of error in the computational results. For this domain, the ratio of the drag force to the applied force on the flow, from the pressure gradient, is less than 1%.

The results of a corresponding direct numerical simulation are also given in Table 1. The simulation was based on a mesh of 2220 hexahedral elements that resolved the geometry of the spheroid and the channel, using larger elements away from the particle. Upon convergence, the integrated drag force on the spheroid is $F_1/(\mu a_2 u_o) = 28.60$ and is consistent with both the theoretical result and the result from FCM. Table 1 also lists the nondimensional fluid torque T_3 on the fixed particle in the shear flow. A positive external torque on the particle is required to prevent rotation in the clockwise sense, based on sketch in Fig. 4. The results of Section 3 may be used to estimate the fluid torque on an isolated spheroid fixed in the shear flow (68) at this location. This nondimensional torque $T_3/(\mu a_2^2 u_o)$ equals -3.026. The FCM and DNS results for the torque match to within approximately 3%. The computational errors in evaluating the torque are in the range of 1–1.5%.

Fig. 5 shows a comparison of the u_1 and u_2 velocity profiles versus inter-wall distance x_2 in the symmetry plane $x_3 = 0$. The Stokes flow is also symmetric about $x_1 = 0$. Upstream, or downstream, of the particle at $x_1 = -4a_2 = -2a_1$ there is good agreement between the FCM and the DNS results. FCM does not match the flow at the stagnation points, at the tip of the spheroid, and here $u_1/u_o \simeq 0.1$.

The flow at finite Reynolds number is computed in a smaller periodic domain with $L_3/a_2 = 5$ and in the streamwise direction the channel size is $-14 \leqslant x_1/a_2 \leqslant 6$. An inflow boundary condition is imposed at $x_1/a_2 = -14$ with the flow velocity specified as (68) and $u_2 = u_3 = 0$. Standard Neumann-type outflow conditions are imposed at $x_1/a_2 = 6$. The Reynolds number based on the approach velocity u_0 and the diameter of the spheroid $2a_2$ is then $Re = 2$. The FCM simulations are based on

Table 1
Summary of fluid forces and torques on a spheroid in Stokes flow, held fixed in a plane Poiseuille flow. The particle is aligned with the flow. Differences in the drag force relative to theory [46] are in parentheses.

Case	$F_1/(\mu a_2 u_o)$	$T_3/(\mu a_2^2 u_o)$
Theory	28.816	
FCM	29.266 (1.56%)	−4.376
DNS	28.598 (0.76%)	−4.230

sentation in each element. The results of DNS are
ial representation. Table 2 provides a comparison
M. There is good agreement for the estimated fluid
is non-zero at finite Reynolds number, reflecting
ignment of the drag force with the ambient flow.
ll compared to the total drag force.
tour levels for the streamwise velocity component
inflow match and provide a reference for compar-
the gap between the particle and the wall is clearly
re is a negative flow region within the particle vol-
nose shown in Figs. 3 and 5. At the upstream stag-
n stagnation point $u_1/u_o \simeq 0.1$. Further details are

the forces and flow associated with an ellipsoidal
section, we consider two examples of an ellipsoid

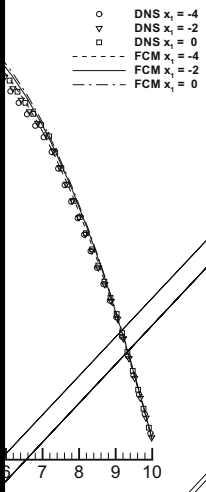

Table 2
Summary of fluid forces and torques on a spheroid held fixed in a plane Poiseuille flow, with the particle aligned with the flow. Particle Reynolds number $Re = 2a_2u_o/\nu$ is 2. Difference relative to DNS is shown as a percentage.

Case	$F_1/(\mu a_2 u_o)$	$F_2/(\mu a_2 u_o)$	$T_3/(\mu a_2^2 u_o)$
DNS	34.23	2.898	−4.120
FCM	34.37 (0.4%)	3.078 (6%)	−4.102 (0.4%)

in a duct with a square cross-section. A Poiseuille flow is driven by an applied pressure gradient. In the first case the ellipsoid is placed near a side-wall and inclined at an angle of 15° to the flow, in the second case the ellipsoid is on the centerline of the duct and inclined at an angle of 45°. The geometry of the duct and the particle dimensions are the same as in Section 5.1. Element meshes are set up in each case and the spectral element representation chosen so as to ensure that the corresponding DNS and FCM simulations are resolved numerically.

For the first case, the particle is centered at $x_1/a = 7$ and $x_2/a = 1.5$ or a distance of $2a$ from the adjacent wall. The centerline velocity at $x_1 = 0$ is used as the reference velocity and $u_{cl} = 0.5565$; the corresponding approach velocity is $u_o = 0.463$. The results for the nondimensional drag force, lift force and torque are given in Table 3 for both Stokes flow and a finite Reynolds number, $Re = 3.9$, based on the duct size, $7a$ and u_{cl}. There is reasonable agreement for the forces and torques. At finite Reynolds number, the drag and torque have changed only slightly while the lift force is reduced by

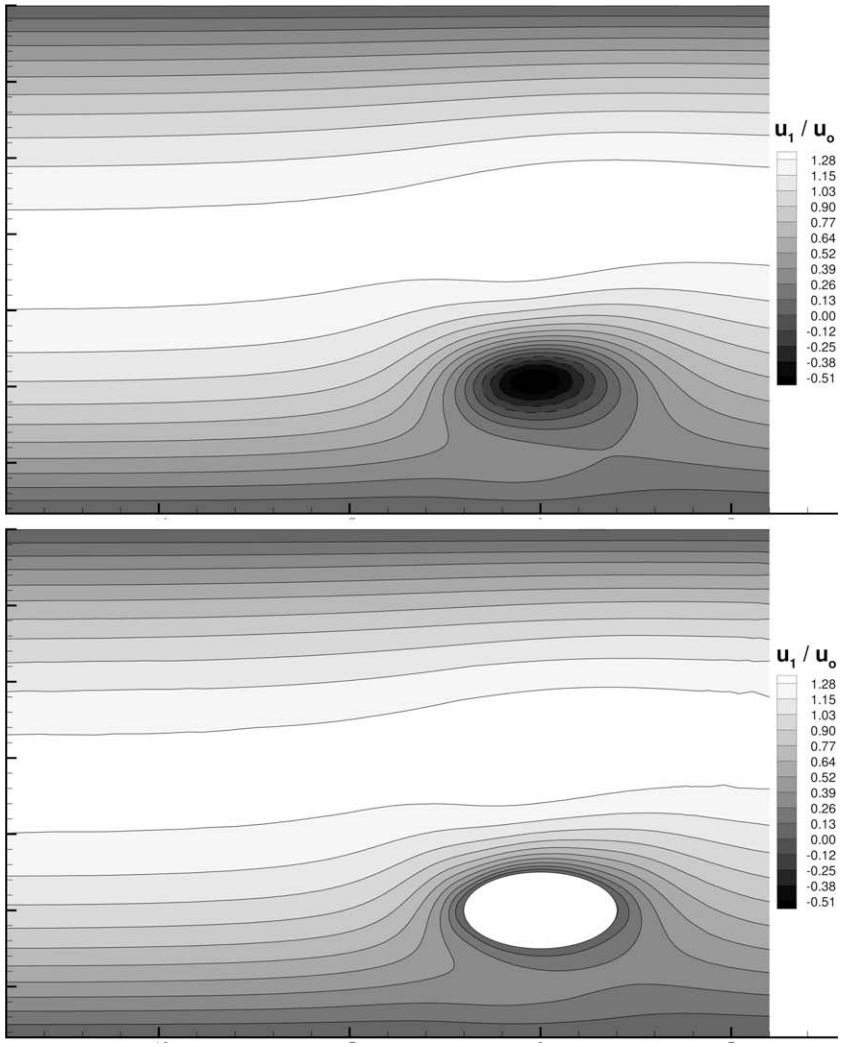

Fig. 6. Spheroid held fixed at $\mathbf{x} = 0$ in Poiseuille flow at $Re = 2$. Comparisons of the u_1 fluid velocity contours in the plane $x_3 = 0$: FCM, top; DNS, bottom. Flow is from left to right.

Table 3
Summary of forces and torques on an ellipsoidal particle held fixed in a Poiseuille flow in a square duct, with the ellipsoid tilted at 15° to the flow. Results are for Stokes flow, $Re = 0$ and for $Re = 3.9$. Results for FCM-MT omit the stresslet term. Difference relative to DNS is shown as a percentage.

Case	Re	$F_1/(\mu a u_{cl})$	$F_2/(\mu a u_{cl})$	$T_3/(\mu a^2 u_{cl})$
DNS	0	35.34	2.182	5.517
FCM	0	37.69 (7%)	2.256 (3%)	5.857 (6%)
DNS	3.9	35.38	1.114	5.325
FCM	3.9	37.84 (7%)	1.092 (2%)	5.591 (5%)
FCM-MT	3.9	38.05 (8%)	1.211 (9%)	6.382 (20%)

about one half. Also at finite Reynolds number, FCM results are given where the stresslet term is omitted and only the torque and force monopole terms are included. Even here, the force estimates are acceptable.

Fig. 7 compares the contours for the streamwise fluid velocity component u_1 computed from DNS and FCM simulations. The figure shows the position of the particle and its orientation relative to the flow, from bottom to top as plotted. Note from the DNS results that the u_1 contours close to the particle are not aligned with the body axes. Outside of the particle domain the contours from DNS and FCM are approximately aligned. As in Fig. 6, the particle is not clearly defined by FCM and the induced flow inside the particle volume is negative. The contours match at the inflow and these, together with the outer two closed contours around the ellipsoid, show the differences in the flow within the gap region.

This reversed flow within the particle volume is an inherent feature of the smoothly varying velocity and vorticity representation of FCM even for spherical particles. This is noted in more detail in [20,21]. The interior flow is similar in qualitative terms to a Hill's spherical vortex. Such a vortex is seen physically when a spherical drop of liquid, held in shape by surface tension, moves with a constant velocity V through a fluid in a Stokes flow. The interior circulation is modified by the ellipsoidal shape of the particle.

In the second case, the ellipsoid is centered in the middle of the channel at $x_1/a = 7$ and $x_2 = x_3 = 0$, tilted at an angle of 45° to the flow. The centerline velocity at $x_1 = 0$ is again used as the reference velocity and $u_{cl} = 0.493$ for the same pressure gradient as in the previous case. Results for both Stokes flow and finite Reynolds flow, $Re = 3.45$, show good agreement between the DNS and FCM results for both forces and torques. In Stokes flow, the torque is exactly zero because of the symmetry of the flow and this is reproduced by FCM while there is a small error in the DNS results. Fig. 8 compares the contours for the fluid velocity component u_1 in the Stokes flow. At the center of the channel the flow around the particle is less influ-

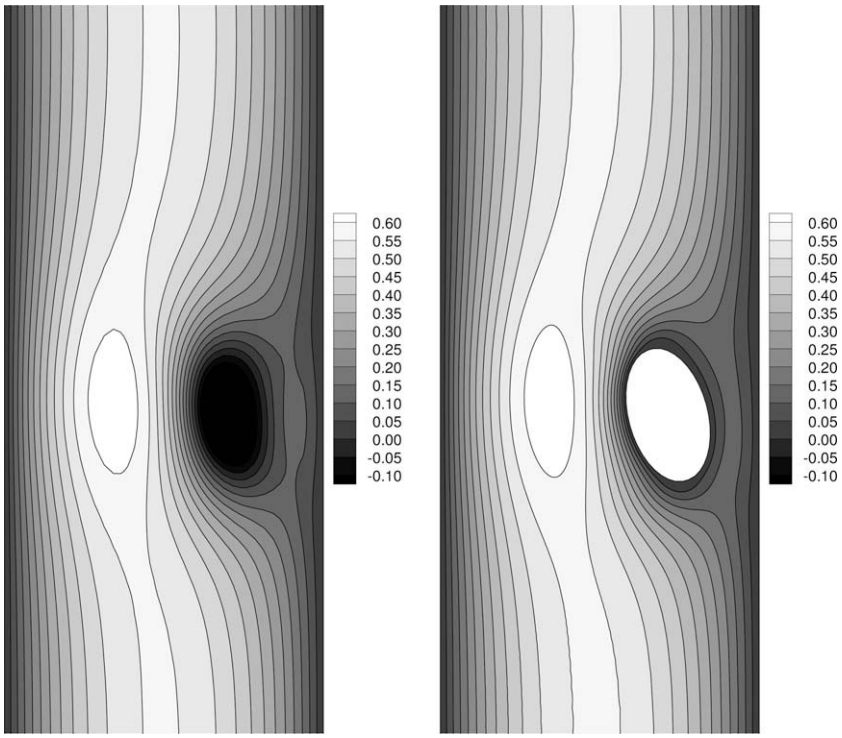

Fig. 7. Ellipsoid, inclined at 15° angle, held fixed in a finite Re Poiseuille flow in a duct, x_1-axis is vertical. Comparisons of contours for streamwise fluid velocity component u_1 in the plane $x_3 = 0$: left, FCM; right, DNS. Note from the DNS results that the u_1 contours are not aligned with the body axes of the ellipsoid.

Fig. 8. Comparisons of contours for streamwise fluid velocity u_1 in plane $x_3 = 0$, ellipsoid at 45° angle in Stokes flow: left, FCM; right, DNS. The x_1-axis is vertical. Note from the DNS results that the u_1 contours are not aligned with the body axes of the ellipsoid.

enced by the walls. There is again a negative velocity inside the particle volume, inherent to the FCM results, but outside the particle domain the contours from FCM match those from DNS except very close to the surface. As in the previous example, the u_1-contours from DNS are not aligned with the axes of the ellipsoid or the body shape.

6. Free motion of ellipsoidal particles

In this section, we consider briefly some examples of the dynamics of freely moving ellipsoidal particles suspended in a fluid. The first example is for sedimentation under gravity in a vertical channel, where a pair of particles interact hydrodynamically as they fall side by side. So as to demonstrate the interaction of ellipsoidal particles, we used FCM to compute the motion of two particles whose semi-axes are $a_1 = 1.5a$, $a_2 = 0.75a$ and $a_3 = 1.0a$. The particles are placed in a vertical channel with rigid parallel planar side-walls at $x_2/a = \pm 8$. The x_1-axis is aligned with the vertical and periodic boundary conditions are applied for both the x_1-direction, $0 \leqslant x_1/a \leqslant 16$, and the spanwise x_3-direction, $-5 \leqslant x_3/a \leqslant 5$. The net force of gravity on each particle is equal to $F_1 = -60\pi$, so that the corresponding force Reynolds number $Re_F = 188.5$. Initially, the particles are introduced either side of the centerline of the channel at $x_2 = \pm 2.5$ and in the plane $x_3 = 0$ with the long axis vertical and shortest axis normal to the side-walls. The flow is initialized by computing first the corresponding Stokes flow for the two particles fixed at these positions and orientations. Following this, at $t = 200$, the particles are released and the full Navier–Stokes equations are solved for the finite Reynolds number flow and to determine the particle motion.

Fig. 9 shows a sketch of the trajectories and the orientations of the two ellipsoidal particles following their release. There is an initial transient stage before a regular periodic motion develops. The particles quickly rotate from their initial vertical alignment to a horizontal alignment. Indeed, a separate simulation of a single particle in the channel shows that it will turn to fall broadside on at a velocity $V_1 = -8.2$, as seen similarly in the results of Pan et al. [39]. The two particles falling side by side each create a shear flow causing the other particle to rotate. Fig. 10 shows the temporal evolution of the velocity and the angular velocity of each particle. Particle 1, on the left of Fig. 9, rotates in a clockwise sense and $\Omega_3 > 0$. As the particles fall, they drift apart as the direction of the settling velocity changes with the particle orientation. The shear flow interactions of the particles weaken as they separate and as their orientation continues to change the particles then drift back towards each other. By $t = 220$ a clear periodic cycle has developed. The average vertical fall speed of the particles is greater than it would be for a single particle. The channel walls have a secondary effect on this observed response as the particles are relatively further from the walls and closer to the centerline. This is in contrast to the motion of a single ellipsoid settling in a narrow tube considered by Swaminathan et al. [40].

The second example is for the motion of a single, neutrally buoyant ellipsoid suspended in a plane Poiseuille shear flow. Segre and Silberberg [52], using a Poiseuille flow through a circular tube, demonstrated experimentally that small, neutrally

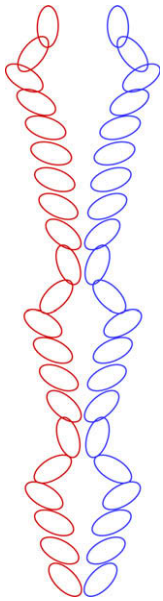

Fig. 9. The sketch of the trajectories and orientations of the two ellipsoidal particles settling side by side in a vertical channel. The scale for the vertical x_1-distance is compressed relative to the horizontal x_2 separation. Particle 1 is on the left, seeded at $x_2/a = -2.5,\ x_3 = 0$; particle 2 is seeded at $x_2/a = 2.5,\ x_3 = 0$.

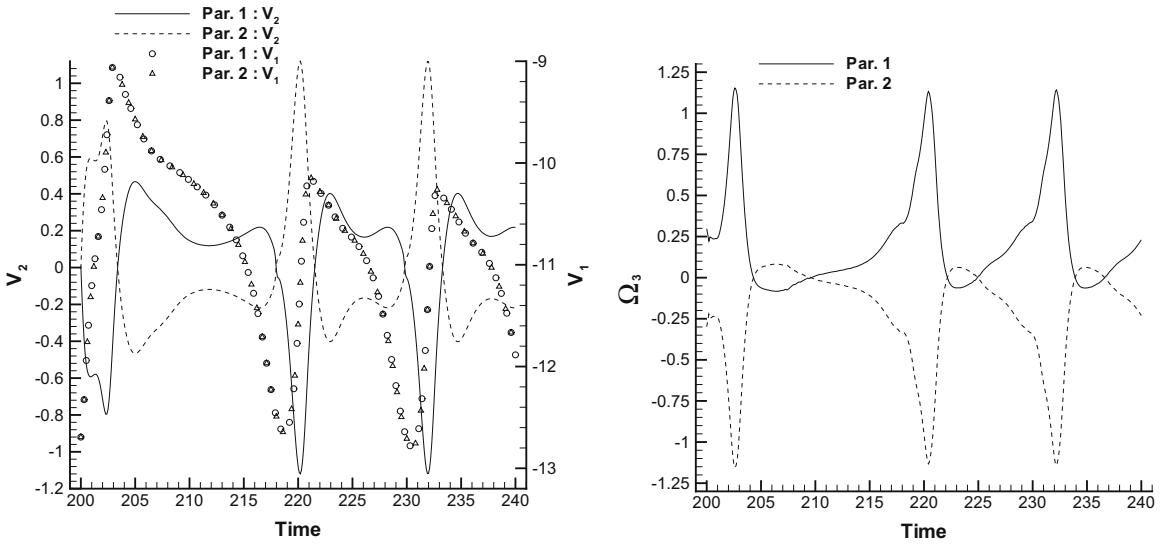

Fig. 10. Two ellipsoidal particles settling vertically, side by side, in a channel: the velocity components (left) and the angular velocity components (right) versus time.

buoyant, rigid spherical particles will migrate laterally to a certain equilibrium position at about 0.6 tube radii from the axis, regardless of the sphere's initial radial position. Theory, developed principally by Schonberg and Hinch [53] and by Asmolov [54], shows that due to the curvature of the velocity profile and the variations of the shear rate across the tube or planar channel that even a neutrally buoyant particle will tend to lag the corresponding fluid velocity at the particle center. This slip velocity results then in a lateral lift force due to fluid inertia effects and there are specific stable equilibrium points where the force vanishes at locations between the centerline and the wall. The precise location depends on the flow Reynolds number and the ratio of the particle diameter to the tube diameter or channel width. These results have been substantiated by results of numerical simulations [55,56] and by experiments [57].

The study of similar effects for ellipsoidal particles is limited. There is the additional parameter of the aspect ratio of the particle and unlike a sphere the hydrodynamic response of an ellipsoid will change as it rotates in the shear flow. Some re-

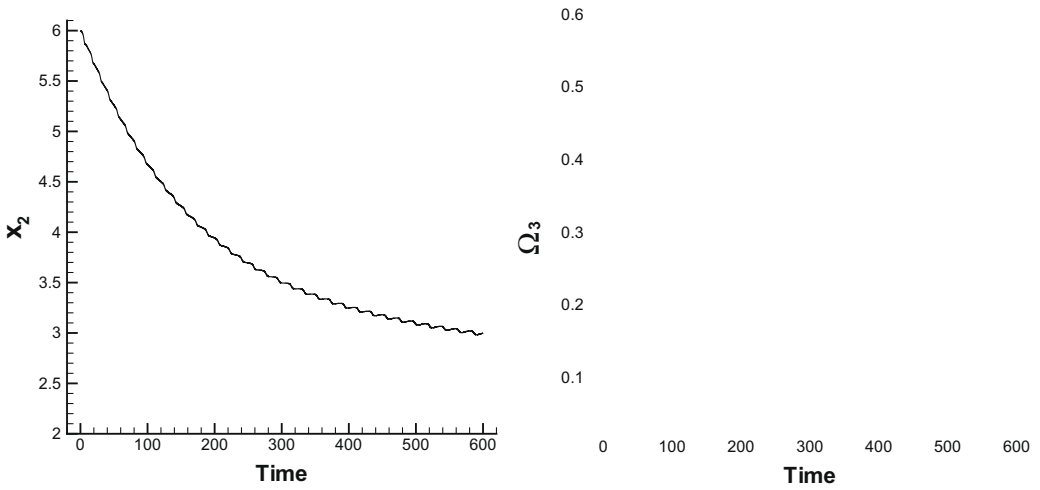

Fig. 11. Temporal evolution of the particle's trajectory in the direction of shear (left), channel walls are at $x_2 = \pm 8$, particle seeded at $x_2 = 6$. Temporal evolution (right) of the particle's angular velocity.

sults on the motion of two-dimensional elliptic particles in planar Poiseuille flow are given by Qi et al. [36] based on numerical simulations with LBM. We show briefly in Fig. 11 some preliminary results for the motion of a three-dimensional ellipsoid in a channel flow obtained from simulations with FCM.

A plane Poiseuille flow is established by applying a pressure gradient to the fluid between planar rigid walls at $x_2/a = \pm 8$. Periodic boundary conditions are applied in the other two directions, with the spanwise direction corresponding to $-5 \leqslant x_3/a \leqslant 5$ and the streamwise direction $0 \leqslant x_1/a \leqslant 14$. The centerline velocity of the flow is $u_{cl} = 4.0$ and the parabolic profile is $u_1 = u_{cl}(1 - x_2^2/64)$, giving a Reynolds number for the channel flow $Re = 32$ based on u_{cl} and the channel half-width. A neutrally buoyant ellipsoid with semi-axes $a_1 = 1.5a,\ a_2 = 0.75a$ and $a_3 = a$ is introduced into the flow near to the upper wall at $x_2 = 6$ with the axes of the particle aligned with channel axes. The simulation uses a nonuniform mesh of 728 hexahedral elements. Fig. 11 shows the temporal evolution of the particle position as it drifts in the x_2-direction form the initial position at $x_2 = 6$ towards a position closer to the centerline at $x_2 \sim 3$. Also shown are the corresponding variations in the angular velocity Ω_3 of the particle. The changing orientation of the particle causes it to fluctuate laterally as it drifts. For the present configuration, if the flow Reynolds number is increased the equilibrium position is closer to the wall, consistent with the two-dimensional results [36].

7. Conclusions

In this paper, we have presented the extension of the force-coupling method to include general ellipsoidal particles. This is achieved by a rescaling of the Gaussian envelope for the particle and using the generalized form (13). In all other respects the method is unchanged and specifically the relations between the envelope scales σ and the particle dimensions are the same as for spherical particles. Analysis shows that the FCM results for the general mobility tensor of a single spheroid in Stokes flow are exact and that the Faxén corrections are approximately correct. The numerical implementation of these methods is discussed and specific comparisons made for prescribed particle motion with full direct numerical simulations for both Stokes flows and low, but non-zero, Reynolds numbers. In general, there is good agreement for the relations between particle forces and torques and the corresponding velocities and angular velocities. As with spherical particles, the details of the flow close to the particle surface are not resolved but are well represented elsewhere. Detailed comparisons of streamwise velocity profiles are given in Sections 5.1 and 5.2 for different flow examples and these illustrate the good agreement between the results obtained from DNS and with FCM. The more qualitative contour plots in Section 5.3 for the streamwise velocity components show again that outside the particle domain the results from DNS and FCM correspond, noting that the u_1-contours are not aligned with the body axes if the particle is not aligned with the flow.

In terms of computational effort, FCM is an effective method for simulating particle motion. All the simulation results presented were computed on a single-processor Linux workstation using the NEKTAR code. The direct numerical simulations required a larger, more detailed mesh fitted to the body geometry. These latter simulations were too large to be accommodated on a standard workstation and had to be computed using a parallel computer. For example, the FCM results of Section 5.3 for the ellipsoid tilted at 15° to the flow required 384 hexahedral elements and took 166 s per time-step on a single Pentium IV processor. The corresponding DNS required 2100 elements and using 64 processors of an IBM SP3 computer took 26 s per time-step, a factor of 10 increase in computational effort. The relative computational costs for FCM relative to DNS have been discussed previously by Dong et al. [58].

The cost of including more particles with FCM are relatively modest and is no greater if the particles move freely in the flow. There is an initial overhead cost to implement FCM for the particle phase but thereafter the computational effort increases linearly with the number of particles, as noted in Section 1. Among the previously reported applications of FCM to flows in random suspension of spherical particles are the studies of platelet aggregation in blood flow by Pivkin et al. [59] and of bidisperse suspensions in a shear flow by Abbas et al. [60]. In the latter study up to 3200 particles, corresponding to a volume fraction of 12%, were simulated with the full FCM and including short-range viscous lubrication forces and particle contact forces. The inclusion of these short-range forces potentially could increase the computational cost to scale with N_P^2, where N_P is the number of particles. Standard, linked-list methods and other procedures reduce these costs significantly [61]. A preliminary study with a suspension of 100 oblate spheroids in a Poiseiulle flow shows the same level of relative computational costs as for spherical particles although the computation of contact forces is more complex for ellipsoids.[1]

The extension of FCM to ellipsoidal particles has been validated for the limit of Stokes flow and has been demonstrated for several examples in finite Reynolds number flows. Previous work [22,24], has demonstrated the validity of FCM for spherical particles in a range of contexts for particle Reynolds numbers up to 12. Useful results may still be obtained for Reynolds numbers up to 20 in certain situations but beyond this flow separation may occur and (3) is not sufficient to represent the flow complexity. In the example of an isolated sphere, rotating about an axis, the secondary flow generated at finite Reynolds number is strongly dependent on the near-surface features of the primary flow and this is only partially resolved by FCM [62]. The important feature of FCM is that it is not limited to Stokes flow conditions, as is the case for standard multipole methods or boundary integral methods, and is able to describe low but finite Reynolds applications.

The present results also point to the limitations of using a single force monopole and force dipole combination to represent an ellipsoidal particle in a general complex shear flow, specifically as the particle aspect ratio increases. This is evident even in Stokes flow as seen from the form of the Faxén corrections (59). The shortest minor axis of the particle may be small compared to the length scale of the flow variation but the major axis may not. With aspect ratios, for example, in the range of 0.5–2, the methods and results have good general accuracy. The numerical resolution required for FCM is set by the smallest semi-axis of the particle. The envelope (13) provides a fairly sharp definition of the particle in this direction. In the direction of the largest semi-axis though the envelope gives a shallower, smoother representation. The spatial resolution required for FCM means that there would be 15–18 grid (or collocation) points along the major axis for a prolate spheroid of aspect ratio 3:1. This available resolution along the major axis though would not be fully utilized. A more effective approach for an elongated particle or fiber would be to use a distribution of FCM multipoles along the body axis to represent the motion in a non-uniform or unsteady flow. This is the approach taken for example in a recent paper describing artificial microswimmers [63]. There are inherent limitations to the use of a multipole representation centered in the particle to describe flow details at the surface, where this is far from the center. Slow convergence means that the inclusion of higher order multipole terms does little to remedy this and is more costly to implement.

Acknowledgments

This work was supported by the National Science Foundation under awards CTS-0326702 and DMS-0506312. The authors wish to thank Sune Lomholt and Kyongmin Yeo for helpful discussions.

Appendix

The components of the tensor A_{ijkm} are evaluated from (34) for the specific case where the symmetry axis **m** is parallel to the x_1-axis and the components are referred the principal axes of the spheroid. The components are then related to the general coefficients α_1—α_6 in (35), making use of the conditions (36). In doing so, it is convenient to introduce intermediate coefficients:

$$\begin{aligned}
&A_{1111} = b_1 = \alpha_1 + 2\alpha_2 - \alpha_4,\\
&A_{2222} = A_{3333} = b_2 = \alpha_1 + 2\alpha_2,\\
&A_{1122} = A_{1133} = b_3 = \alpha_1 + \alpha_5,\\
&A_{2211} = A_{3311} = b_4 = \alpha_1 + \alpha_3,\\
&A_{2233} = A_{3322} = b_5 = \alpha_1,\\
&A_{1212} = A_{1313} = b_6 = \alpha_2 + \alpha_4,\\
&A_{2323} = (b_2 - b_5)/2 = \alpha_2.
\end{aligned} \tag{A.1}$$

The evaluation procedure is similar to that used to determine the mobility coefficients in (25), reducing the results to integrals in $t = k_1/k$.

The value of A_{1111} is

[1] K. Yeo, Private communication, 2008.

$$b_1 = -\frac{1}{16\pi^{3/2}\mu\sigma_2^3}\int_{-1}^{1}\frac{(1-t^2)t^2}{(1+(\lambda^2-1)t^2)^{3/2}}dt. \tag{A.2}$$

This may be expressed in terms of the standard integrals

$$\begin{aligned} I_0 &= \int_{-1}^{1}\frac{1}{[1+(\lambda^2-1)t^2]^{3/2}}dt,\\ I_1 &= \int_{-1}^{1}\frac{t^2}{[1+(\lambda^2-1)t^2]^{3/2}}dt,\\ I_2 &= \int_{-1}^{1}\frac{t^4}{[1+(\lambda^2-1)t^2]^{3/2}}dt, \end{aligned} \tag{A.3}$$

and the constant $C = 1/\{32\pi^{3/2}\mu\sigma_2^3\}$ as

$$b_1 = -2C\{I_1 - I_2\}. \tag{A.4}$$

The other coefficients may be found in the same manner as

$$\begin{aligned} b_2 &= -C\left\{\frac{1}{4}I_0 + \frac{1}{2}I_1 - \frac{3}{4}I_2\right\},\\ b_3 &= -C\{I_0 - 2I_1 + I_2\},\\ b_4 &= -C\{I_1 + I_2\},\\ b_5 &= -C\left\{\frac{3}{4}I_0 - \frac{1}{2}I_1 - \frac{1}{4}I_2\right\},\\ b_6 &= C\{I_1 - I_2\}. \end{aligned} \tag{A.5}$$

As a result of (6) the constant $C = 3/(16\pi\mu a_2^3)$.

With the aspect ratio $\lambda = a_1/a_2 = \sigma_1/\sigma_2$, the value of the integrals (A.3) are

$$\begin{aligned} I_0 &= \frac{2}{\lambda},\\ I_1 &= -\frac{2}{\tau^3}\left(\frac{\tau}{\lambda} - \log(\lambda+\tau)\right),\\ I_2 &= \frac{1}{\tau^5}\left((\lambda^2+2)\frac{\tau}{\lambda} - 3\log(\lambda+\tau)\right), \end{aligned} \tag{A.6}$$

for prolate spheroids, $\lambda > 1$, with $\tau^2 = |\lambda^2 - 1|$. For oblate spheroids, $\lambda < 1$,

$$\begin{aligned} I_0 &= \frac{2}{\lambda},\\ I_1 &= \frac{2}{\tau^3}\left(\frac{\tau}{\lambda} - \tan^{-1}(\tau/\lambda)\right),\\ I_2 &= \frac{1}{\tau^5}\left((\lambda^2+2)\frac{\tau}{\lambda} - 3\tan^{-1}(\tau/\lambda)\right). \end{aligned} \tag{A.7}$$

In addition, the integrals are related and

$$\begin{aligned} &I_0 - 3I_1 - 2\tau^2 I_2 = 0 \quad \text{for } \lambda > 1,\\ &I_0 - 3I_1 + 2\tau^2 I_2 = 0 \quad \text{for } \lambda < 1. \end{aligned} \tag{A.8}$$

The coefficients α_1–α_6 in (35) are given by

$$\begin{aligned} \alpha_1 &= C\left[\frac{1}{4}I_2 + \frac{1}{2}I_1 - \frac{3}{4}I_0\right],\\ \alpha_2 &= C\left[\frac{1}{4}I_2 - \frac{1}{2}I_1 + \frac{1}{4}I_0\right],\\ \alpha_3 &= C\left[-\frac{5}{4}I_2 - \frac{3}{2}I_1 + \frac{3}{4}I_0\right],\\ \alpha_4 &= C\left[-\frac{5}{4}I_2 + \frac{3}{2}I_1 - \frac{1}{4}I_0\right],\\ \alpha_5 &= C\left[-\frac{5}{4}I_2 + \frac{3}{2}I_1 - \frac{1}{4}I_0\right],\\ \alpha_6 &= C\left[\frac{35}{4}I_2 - \frac{15}{2}I_1 + \frac{3}{4}I_0\right]. \end{aligned} \tag{A.9}$$

References

[1] C.-M. Ho, Y.-C. Tai, Micro-electro-mechanical-systems (MEMS) and fluid flows, Annu. Rev. Fluid Mech. 30 (1998) 579–612.
[2] P. Telleman, U. Larsen, J. Philip, G. Blankenstein, A. Wolff, Cell sorting in microfluidic systems, in: Harrison, van den Berg (Eds.), Micro Total Analysis Systems'98, Kluwer, Dordrecht, 1998, pp. 39–44.
[3] R.A.J. Squier Jr., T. Vestad, J. Oakey, D. Marr, P. Bado, M. Dugan, A. Said, Microfluidics sorting system based on optical waveguide integration and diode laser bar trapping, Lab. Chip 6 (2006) 422–426.
[4] M. Hayes, N. Polson, A. Garcia, Active control of dynamic supraparticle structures in microchannels, Langmuir 17 (2001) 2866–2871.
[5] P. Doyle, J. Bibette, A. Bancaud, J.-L. Viory, Self-assembled magnetic matrices for DNA separation chips, Science 295 (2002) 2237.
[6] R. Haghgooie, P. Doyle, Transition from two-dimensional to three-dimensional behavior in the self-assembly of magnetorheological fluids confined in thin slits, Phys. Rev. E 75 (2007) 061406.
[7] A. Terray, J. Oakey, D. Marr, Microfluidic control using colloidal devices, Science 296 (2002) 1841–1843.
[8] S. Bleil, D. Marr, C. Bechinger, Field-mediated self-assembly and actuation of highly parallel microfluidic devices, Appl. Phys. Lett. 88 (2006) 263515.
[9] D. Liu, M. Maxey, G. Karniadakis, Modeling and optimization of colloidal micro-pumps, J. Micromech. Microeng. 14 (2004) 567–575.
[10] G. Karniadakis, A. Beskok, N. Aluru, Microflows and Nanoflows: Fundamentals and Simulation, Springer, New York, 2005.
[11] J. Brady, G. Bossis, Stokesian dynamics, Annu. Rev. Fluid Mech. 20 (1988) 111–157.
[12] A. Sierou, J. Brady, Accelerated Stokesian dynamics simulations, J. Fluid Mech. 448 (2001) 115–146.
[13] H. Hu, Direct simulation of flows of solid–liquid mixtures, Int. J. Multiphase Flow 22 (1996) 335–352.
[14] A. Johnson, T. Tezduyar, 3D Simulation of fluid particle interactions with the number of particles reaching 100, Comput. Method Appl. Mech. Eng. 145 (1997) 301–321.
[15] H. Hu, N. Patankar, M. Zhu, Direct numerical simulation of solid–liquid systems using the arbitrary Lagrangian–Eulerian technique, J. Comput. Phys. 169 (2001) 427–462.
[16] C. Aidun, Y. Lu, Lattice-Boltzmann simulation of solid particles suspended in fluid, J. Stat. Phys. 81 (1995) 49–61.
[17] A. Ladd, R. Verberg, Lattice-Boltzmann simulations of particle–fluid suspensions, J. Stat. Phys. 104 (2001) 1191–1251.
[18] R. Glowinski, T. Pan, T. Hesla, D. Joseph, J. Periaux, A fictitious domain approach to the direct numerical simulation of incompressible viscous flow past moving rigid bodies: application to particulate flow, J. Comput. Phys. 169 (2001) 363–426.
[19] N. Patankar, P. Singh, D. Joseph, R. Glowinski, T. Pan, A new formulation of the distributed lagrange multiplier/fictitious domain method for particulate flows, Int. J. Multiphase Flow 26 (2000) 1509–1524.
[20] M. Maxey, B. Patel, Localized force representations for particles sedimenting in stokes flow, Int. J. Multiphase Flow 27 (2001) 1603–1626.
[21] S. Lomholt, M. Maxey, Force coupling method for particles sedimenting in a channel: Stokes flow, J. Comput. Phys. 184 (2003) 381–405.
[22] D. Liu, M. Maxey, G. Karniadakis, A fast method for particulate microflows, J. Microelectromech. Syst. 11 (2002) 691–702.
[23] S. Lomholt, B. Stenum, M. Maxey, Experimental verification of the force coupling method for particulate flows, Int. J. Multiphase Flow 28 (2002) 225–246.
[24] D. Liu, Spectral Element/Force Coupling Method: Application to Colloidal Micro-Devices and Self-Assembly Structures in 3D Complex-Geometry Domains, Ph.D. Thesis, Brown University, 2004.
[25] D. Saintillan, E. Shaqfeh, E. Darve, The growth of concentration fluctuations in dilute dispersions of orientable and deformable particles under sedimentation, J. Fluid Mech. 553 (2006) 347–388.
[26] D. Koch, E. Shaqfeh, The instability of a dispersion of sedimenting spheroids, J. Fluid Mech. 209 (1989) 521–542.
[27] G. Jeffery, The motion of ellipsoidal particles immersed in a viscous fluid, Proc. R. Soc. Lond. Ser. A 102 (1922) 161–179.
[28] R. Mallier, M. Maxey, The settling of nonspherical particles in a cellular flow field, Phys. Fluid A 3 (1991) 1481–1494.
[29] H. Shin, M. Maxey, Chaotic motion of nonspherical particles settling in a cellular flow field, Phys. Rev. E 56 (1997) 5431–5444.
[30] I. Claeys, J. Brady, Suspensions of prolate spheroids in Stokes flow. Part 1. Dynamics of a finite number of particles in an unbounded fluid, J. Fluid Mech. 251 (1993) 411–442.
[31] C. Pozrikidis, Orbiting motion of a freely suspended spheroid near a plane wall, J. Fluid Mech. 541 (2005) 105–114.
[32] C. Pozrikidis, Interception of two spheroidal particles in shear flow, J. Non-Newt. Fluid Mech. 136 (2006) 50–63.
[33] M. Staben, A. Zinchenko, R. Davis, Dynamics simulation of spheroid motion between two parallel plane walls in low-Reynolds-number Poiseuille flow, J. Fluid Mech. 553 (2006) 187–226.
[34] N. Mody, M. King, Three-dimensional simulations of a platelet-shaped spheroid near a wall in a shear flow, Phys. Fluid 17 (2005) 113302.
[35] C. Aidun, Y. Lu, E. Ding, Direct analysis of particulate suspensions with inertia using the discrete Boltzmann equation, J. Fluid Mech. 373 (1998) 287–311.
[36] D. Qi, L. Luo, R. Aravamuthan, W. Strieder, Lateral migration and orientation of elliptical particles in Poiseuille flows, J. Stat. Phys. 107 (2002) 101–120.
[37] J. Feng, H. Hu, D. Joseph, Direct simulation of initial value problems for the motion of solid bodies in a Newtonian fluid. Part 1. Sedimentation, J. Fluid Mech. 261 (1994) 95–134.
[38] D. Qi, L. Luo, Rotational and orientational behavior of three-dimensional spheroidal particles in Couette flows, J. Fluid Mech. 477 (2003) 201–213.
[39] T.-W. Pan, R. Glowinski, G. Galdi, Direct simulation of the motion of settling ellipsoid in Newtonian fluid, J. Comput. Appl. Math. 149 (2002) 71–82.
[40] T. Swaminathan, K. Mukundakrishnan, H. Hu, Sedimentation of an ellipsoid inside an infinitely long tube at low and intermediate Reynolds numbers, J. Fluid Mech. 551 (2006) 357–385.
[41] Z. Zhang, A. Prosperetti, A second-order method for three-dimensional particle simulation, J. Comput. Phys. 210 (2005) 292–324.
[42] C. Peskin, The immersed boundary method, Acta Numer. 11 (2002) 479–517.
[43] M. Uhlmann, An immersed boundary method with direct forcing for the simulation of particulate flows, J. Comput. Phys. 209 (2005) 448–476.
[44] N. Sharma, N. Patankar, A fast computation technique for the direct numerical simulation of rigid particulate flows, J. Comput. Phys. 205 (2005) 439–457.
[45] H. Lamb, Hydrodynamics, sixth ed., Cambridge University Press, 1932.
[46] J. Happel, H. Brenner, Low Reynolds Number Hydrodynamics, Martinus Nijhoff, 1986.
[47] S. Kim, S. Karrila, Microhydrodynamics, Principles and Selected Applications, Butterworth–Heinemann, 1991.
[48] J. Rallison, Note on the Faxén relations for a particle in Stokes flow, J. Fluid Mech. 88 (1978) 529–533.
[49] H. Brenner, The Stokes resistance of an arbitrary particle – IV. Arbitrary fields of flow, Chem. Eng. Sci. 19 (1964) 703–727.
[50] G. Karniadakis, S. Sherwin, Spectral/hp Element Methods for Computational Fluid Dynamics, Oxford University Press, 2005.
[51] S. Dance, M. Maxey, Incorporation of lubrication effects into the force-coupling method for particulate two-phase flow, J. Comput. Phys. 189 (2003) 212–238.
[52] G. Segre, A. Silberberg, Behavior of macroscopic rigid spheres in Poiseuille flow, Part 1 and Part 2, J. Fluid Mech. 14 (1962) 115–157.
[53] J. Schonberg, E. Hinch, Inertial migration of a sphere in Poiseuille flow, J. Fluid Mech. 203 (1989) 517–524.
[54] E. Asmolov, The inertial lift on a spherical particle in a plane Poiseuille flow at large channel Reynolds numbers, J. Fluid Mech. 381 (1999) 63–87.
[55] B. Yang, J. Wang, D. Joseph, H. Hu, T.-W. Pan, R. Glowinski, Migration of a sphere in tube flow, J. Fluid Mech. 540 (2005) 109–131.
[56] B. Chun, A. Ladd, Inertial migration of neutrally buoyant particles in a square duct: an investigation of multiple equilibrium positions, Phys. Fluid 18 (2006) 031704.
[57] J.-P. Matas, J. Morris, E. Guazelli, Inertial migration of rigid spherical particles in Poiseuille flow, J. Fluid Mech. 515 (2004) 171–195.
[58] S. Dong, D. Liu, M. Maxey, G. Karniadakis, Spectral distributed lagrange multiplier method: algorithm and benchmark test, J. Comput. Phys. 195 (2004) 695–717.

[59] I. Pivkin, P. Richardson, G. Karniadakis, Blood flow velocity effects and role of activation delay time on growth and form of platelet thrombi, Proc. Natl. Acad. Sci. USA 103 (2006) 17164–17169.
[60] M. Abbas, E. Climent, O. Simonin, M. Maxey, Dynamics of bidisperse suspensions under stokes flows: linear shear flow and sedimentation, Phys. Fluid 18 (2006) 121504.
[61] M. Allen, D. Tildesley, Computer Simulation of Liquids, Clarendon Press, 1994.
[62] X. Luo, M. Maxey, G. Karniadakis, Smoothed profile method for particulate flows: error analysis and simulations, J. Comput. Phys. 228 (2009) 1750–1769.
[63] E. Keaveny, M. Maxey, Spiral swimming of an artificial micro-swimmer, J. Fluid Mech. 598 (2008) 293–319.